Monthly Notices
of the
ROYAL ASTRONOMICAL SOCIETY

Mon. Not. R. Astron. Soc. **416,** 801–816 (2011) doi:10.1111/j.1365-2966.2011.18497.x

X-ray mass proxies from hydrodynamic simulations of galaxy clusters – I

D. Fabjan,[1,2,9★] S. Borgani,[2,3,4★] E. Rasia,[5★] A. Bonafede,[6★] K. Dolag,[7,10★] G. Murante[3,8★] and L. Tornatore[2,3,4★]

[1]*Center of Excellence SPACE-SI, Aškerčeva 12, 1000 Ljubljana, Slovenia*
[2]*Dipartimento di Fisica dell'Università di Trieste, Sezione di Astronomia, via Tiepolo 11, I-34131 Trieste, Italy*
[3]*INAF – Osservatorio Astronomico di Trieste, via Tiepolo 11, I-34131 Trieste, Italy*
[4]*INFN – Istituto Nazionale di Fisica Nucleare, Trieste, Italy*
[5]*Department of Astronomy, University of Michigan, 500 Church St., Ann Arbor, MI 48109, USA*
[6]*Jacobs University Bremen, Campus Ring 1, 28759 Bremen, Germany*
[7]*Universitäts-Sternwarte München, Scheinerstr. 1, D-81679 München, Germany*
[8]*INAF – Osservatorio Astronomico di Torino, Str. Osservatorio 25, I-10025 Pino Torinese, Torino, Italy*
[9]*Faculty of Mathematics and Physics, University of Ljubljana, Jadranska 19, 1000 Ljubljana, Slovenia*
[10]*Max-Planck-Institut für Astrophysik, PO Box 1317, 85741 Garching bei München, Germany*

Accepted 2011 February 7. Received 2010 December 20

ABSTRACT

Using extended sets of cosmological hydrodynamical simulations of galaxy clusters, we present a detailed study of scaling relations between total cluster mass and three mass proxies based on X-ray observable quantities: temperature of the intracluster medium (ICM), gas mass and the product of the two, $Y_X = M_{\rm gas}T$. Our analysis is based on two sets of high-resolution hydrodynamical simulations performed with the TreePM–SPH GADGET code. The first set includes about 140 clusters with masses above $5 \times 10^{13}\,h^{-1}\,{\rm M}_\odot$, with 30 such clusters having mass above $10^{15}\,h^{-1}\,{\rm M}_\odot$. All such clusters have been simulated in two flavours, both with non-radiative physics and including cooling, star formation, chemical enrichment and the effect of supernova feedback triggering galactic ejecta. The extensive statistics offered by this set of simulated clusters is used to quantify the robustness of the scaling relations between mass proxies and total mass, to determine their redshift evolution and to calibrate their intrinsic scatter and its distribution. Furthermore, we use a smaller set of clusters including 18 haloes with masses above $5 \times 10^{13}\,h^{-1}\,{\rm M}_\odot$, four of which are more massive than $10^{15}\,h^{-1}\,{\rm M}_\odot$, to test the robustness of mass proxies against change in the physical processes that are included in the simulations to describe the evolution of the intracluster medium. Each cluster is simulated in seven different flavours to study the effects of (i) thermal conduction, (ii) artificial viscosity, (iii) cooling and star formation, (iv) galactic winds and (v) active galactic nucleus (AGN) feedback.

As a general result, we find the M–$Y_{\rm X}$ scaling relation to be the least sensitive to variations in the ICM physics, its slope and redshift evolution always being very close to the predictions of the self-similar model. As regards the scatter around the best-fitting relations, its distribution is always close to a log-normal one. $M_{\rm gas}$ is the mass proxy with the smallest scatter in mass, with values of $\sigma_{\ln M} \simeq 0.04$–$0.06$ depending on the physics included in the simulation and with a mild dependence on redshift. In terms of the mass–temperature relation, it is the one with the largest scatter, with $\sigma_{\ln M} \gtrsim 0.1$ at $z = 0$ increasing to $\gtrsim 0.15$ at $z = 1$. The intrinsic scatter in the M–$Y_{\rm X}$ relation is slightly larger than that in the M–$M_{\rm gas}$ relation, with $\sigma_{\ln M} \simeq 0.06$ at $z = 0$ and 0.08 at $z = 1$. These results confirm that both $Y_{\rm X}$ and $M_{\rm gas}$ mass proxies are well suited for cosmological applications in future large X-ray surveys. As a word of caution, we point out that

★E-mail: dunja.fabjan@space.si (DF); borgani@oats.inaf.it (SB); rasia@umich.edu (ER); a.bonafede@jacobs-university.de (AB); kdolag@mpa-garching.mpg.de (KD); murante@oato.inaf.it (GM); tornatore@oats.inaf.it (LT)

the analysis presented in this paper does not include the observational effects expected when measuring temperature by fitting X-ray spectra and gas mass from X-ray surface-brightness profiles. A detailed assessment of such effects will be the subject of a forthcoming paper.

Key words: methods: numerical – cosmology: miscellaneous – X-rays: galaxies: clusters.

1 INTRODUCTION

Measuring the mass of galaxy clusters represents the most important aspect of the use of such structures as tracers of cosmic evolution. The cosmological parameters depend, indeed, on the evolution of cluster mass function and on large-scale clustering properties (Borgani et al. 2001; Schuecker et al. 2002; Voit 2005a; Vikhlinin et al. 2009a; Mantz et al. 2010). Restricting the discussion to X-ray observations, to estimate cluster masses we need to assume that the intracluster medium (ICM) sits in hydrostatic equilibrium within the cluster potential well, which is generally assumed to have spherical symmetry. Further, we need to obtain gas density and temperature profiles from high-quality X-ray data. Limits on this approach are represented not only by the strong assumptions made but also by the difficulty of obtaining data of sufficient quality. This is especially true for distant clusters, at $z \gtrsim 0.5$, for which observations of the needed sensitivity would be prohibitively expensive in terms of required exposure time.

To overcome this problem one generally resorts to the observational determinations of mass proxies, i.e. of suitably observable quantities easier to measure and related to total cluster mass through so-called 'scaling relations'. Ideally, a robust mass proxy should be characterized by a low intrinsic scatter with cluster mass, implying that it needs to be relatively insensitive to the cluster dynamical state. Different examples of X-ray mass proxies have been used over the last decade to derive cosmological constraints from X-ray cluster surveys. The easiest-to-measure mass proxy is the total X-ray luminosity, $L_{\rm X}$. While this quantity is known to correlate with cluster mass (Reiprich & Böhringer 2002; Pratt et al. 2009), the $L_{\rm X}$–M relation has a fairly large scatter of about 40 per cent due to the sensitivity of X-ray luminosity to the details of the gas distribution in central regions and therefore to the dynamical state of the cluster. Other commonly adopted choices of mass proxies are the X-ray temperature $T_{\rm X}$ (Henry & Arnaud 1991; Markevitch 1998; Ikebe et al. 2002; Pierpaoli et al. 2003) and the cluster gas mass $M_{\rm gas}$ (Vikhlinin et al. 2003; Voevodkin & Vikhlinin 2004). In order to estimate these quantities, detailed X-ray brightness profiles must be obtained, requiring longer exposure times than those required for $L_{\rm X}$ only. However, they are expected to be more robustly linked to total collapsed mass.

In this context, cosmological hydrodynamical simulations are playing an increasingly relevant role in calibrating the mass proxies, understanding the systematics of cluster mass measurements and defining new mass proxies. Simulations provide the most advanced theoretical tool to capture the complexity of the hierarchical build-up of galaxy clusters and of gas-dynamical processes (see e.g. Borgani & Kravtsov 2009, for a recent review of cluster simulations). A typical example is provided by the role that simulations played in the last few years in calibrating the expected level of violation of hydrostatic equilibrium induced by the presence of non-thermalized gas motions (Rasia, Tormen & Moscardini 2004; Nagai, Vikhlinin & Kravtsov 2007a; Jeltema et al. 2008; Ameglio et al. 2009; Piffaretti & Valdarnini 2008; Lau, Kravtsov & Nagai 2009). Another example is given by the application of simulations in the study of the accuracy of X-ray temperature and gas mass as tracers of the total cluster mass (Bartelmann & Steinmetz 1996; Evrard, Metzler & Navarro 1996; Ettori et al. 2004; Muanwong, Kay & Thomas 2006; Nagai, Kravtsov & Vikhlinin 2007b). With the increasing numerical resolution and degree of realism of the physical processes included, these calibrations are becoming trustworthy, as convincingly shown by different works. A good match between simulations and observations was shown for temperature profiles of clusters (Loken et al. 2002; Borgani et al. 2004; Kay et al. 2007; Nagai et al. 2007b; Leccardi & Molendi 2008), gas density profiles (Roncarelli et al. 2006; Croston et al. 2008) and pressure density (Arnaud et al. 2010).

These comparisons are mostly restricted to the region within R_{500},[1] after excluding the central regions affected by the complex physical processes regulating the 'cool core' structure of the ICM.

For the cluster mass proxies, simulations predict that the $T_{\rm X}$–M relation has an intrinsic scatter that is quite sensitive to the presence of substructures in the ICM and to the cluster dynamical state (O'Hara et al. 2006; Yang, Ricker & Sutter 2009). The gas mass proxy is instead expected to be less sensitive to the cluster dynamical state, thus implying a smaller scatter in its scaling relation with total mass. Moreover it has the advantage that it can be essentially measured from X-ray imaging alone. There is however a caveat, since the dependence of gas mass fraction on cluster mass, clustercentric distance and redshift is not yet completely understood (Ettori et al. 2006).

Kravtsov, Vikhlinin & Nagai (2006) introduced the X-ray equivalent of the integrated Sunyaev–Zeldovich (SZ) flux, the $Y_{\rm X}$ parameter, defined as the product of the gas mass with the cluster temperature. From a set of 16 simulated galaxy clusters these authors found it to be a low-scatter (5–8 per cent) mass proxy, due to the anticorrelation of the residuals in the scaling relation of temperature and gas mass with total mass. Furthermore, the scaling of $Y_{\rm X}$ with total mass was found to be in close agreement with the prediction of the simple self-similar model, based on the assumption that gas follows dark matter and gravitational effects only determine the thermal content of the ICM (Kaiser 1986). The $Y_{\rm X}$–M relation is relatively insensitive to cluster mergers, a result that was independently verified by Poole et al. (2007) and by Rasia et al. (2011) with simulations of cluster mergers. A number of recent observational works estimated Y_X and its correlation with X-ray luminosity. Data from both *XMM–Newton* (Pratt et al. 2009) and the *Chandra* telescope (Maughan 2007; Vikhlinin et al. 2009a) showed that the observed $Y_{\rm X}$–M relation has slope and redshift evolution in agreement with the predictions of the self-similar model. With their samples of both nearby and distant clusters out to $z \sim 1$, these observations confirm that gravitational processes are indeed responsible for the bulk of the total thermal content of galaxy clusters.

A more recent analysis of scaling relations for simulated galaxy clusters presented by Stanek et al. (2010) did not confirm the anticorrelation of the residuals of M–$M_{\rm gas}$ and M–$T_{\rm mw}$. They found that the lowest-scatter mass proxy is $M_{\rm gas}$. A similar result was also

[1] We define M_Δ as the mass contained within the radius R_Δ encompassing an overdensity of Δ times the cosmic critical density, $\rho_c(z) = 3H(z)^2/8\pi G$.

found by Okabe et al. (2010), who computed the scaling relation between X-ray mass proxies and the total cluster mass obtained from lensing observations of 12 clusters at $z \sim 0.2$. From their analysis the conclusion is that $M_{\rm gas}$ has the lowest intrinsic scatter of $\sim$10 per cent with respect to the $\sim$ 20 per cent of the $Y_{\rm X}$ proxy.

At present, $T_{\rm X}, M_{\rm gas}$ and $Y_{\rm X}$ are considered the most robust indicators of cluster mass and, in fact, the most recent cosmological applications of X-ray cluster surveys have been based on the use of such mass proxies (Henry et al. 2009; Vikhlinin et al. 2009b; Mantz et al. 2010).

Ideally, rather than relying on simulations, it would be preferable to calibrate mass proxies directly from observational data. An observational calibration, while possible in principle, requires highly precise measurements of cluster mass in a way that is completely independent of X-ray observations, e.g. from gravitational lensing or from the study of the cluster internal dynamics as traced by member galaxies. Indeed, any determination of the scatter between any of the above three X-ray mass proxies and cluster mass based on the application of hydrostatic equilibrium would be inconclusive, owing to the fact that the relation is between two highly correlated quantities. On the other hand, precise measurements of lensing masses are now available only for a relatively small number of objects (Mahdavi et al. 2008; Okabe et al. 2010; Zhang et al. 2010). Although progress in this direction is expected in the future, today simulations represent a valid alternative with which to calibrate mass proxies and to understand their robustness.

A careful study of mass proxies through simulations requires a large enough sample of clusters simulated both with adequate resolution and by including a range of physical processes. The most direct way to achieve large statistics of clusters would be to carry out simulations of large cosmological boxes (Borgani et al. 2004; Gottloeber et al. 2006; Kay et al. 2007; Burns et al. 2008; Hartley et al. 2008). However, these simulations have to compromise severely as regards box size, achievable resolution and the detail with which different physical processes (e.g. star formation and feedback from different sources) can be studied. As an alternative, one could simulate at high resolution only specific regions surrounding clusters that have previously been identified from low-resolution simulations of large cosmological volumes. The advantage of this approach is that it can provide a more realistic numerical description, in terms of resolution reached and physical processes included, within only the 'zoomed-in' Lagrangian regions surrounding clusters. As a matter of fact, this resimulation procedure is non-trivial to implement, thus limiting the statistics of resimulated clusters so far presented in the literature. For instance, Dolag et al. (2009) presented a set of 18 such clusters, of which however only four have $M_{200} > 10^{15}\,h^{-1}\,{\rm M}_{\odot}$ (see also Fabjan et al. 2010). Puchwein, Sijacki & Springel (2008) and Lau et al. (2009) presented sets of resimulated clusters of comparable size, again with only a couple of them being as massive as $\sim 10^{15}\,h^{-1}\,{\rm M}_{\odot}$.

In this paper we use two sets of simulated clusters, the combination of which provides us with both extensive statistics of massive objects and a range of physical processes over which to test the stability of the scaling relations. The first set of clusters (Set 1 hereafter) contains about 140 clusters, 30 of which have masses larger than $10^{15}\,h^{-1}\,{\rm M}_{\odot}$. For all of them, we carried out simulations both with non-radiative physics and including cooling, star formation and galactic winds powered by Type II supernova (SN II) explosions. The second set of simulations (Set 2 hereafter) includes 18 clusters, with four of them having masses larger than $10^{15}\,h^{-1}\,{\rm M}_{\odot}$. We refer to Dolag et al. (2009) for a complete description of the second set of simulations. This smaller set of simulated clusters complements the first set, since it has been simulated by changing the description of physical processes (e.g. artificial viscosity, cooling, star formation, feedback efficiency from SN and gas accretion on to supermassive black holes) in seven different ways. The complementary analysis of these two cluster sets allows us to address in detail the stability and robustness of the calibration of X-ray mass proxies with simulations, by combining statistics of massive haloes, numerical resolution and the range of physical processes included.

In this first paper we will carry out an analysis of the scaling relation of the mass proxies against mass by neglecting all observational effects. For this reason ICM temperature will be mass-weighted (where not listed differently) and all quantities will be estimated using a three-dimensional analysis without including projection effects. In this way, we will assess the intrinsic performance of $T_{\rm X}$, $M_{\rm gas}$ and $Y_{\rm X}$ as tracers of the true mass, while we defer to a forthcoming paper (Rasia et al., in preparation) for a detailed analysis of the impact of observational biases.

This paper is organized as follows. We present in Section 2 the simulations analysed in this paper. After a description of the GADGET simulation code (Springel 2005) and the physical processes included in the simulations, we describe the initial conditions and the general characteristics of the resulting samples of simulated clusters. In Section 3 we present the results of our analysis. After introducing the definitions of mass proxies we present results at $z = 0$, along with an assessment of the dependence of the scaling relations on the physical processes included in the simulations. We finally discuss the evolution of scaling relations and their intrinsic scatter with redshift. We discuss our results and summarize the main conclusions of our analysis in Section 4.

2 SIMULATIONS

2.1 The simulation code and adopted physical models

In this section we introduce the simulation code and all the different physical processes considered in resimulating our objects. Simulations have been carried out using the Tree–PM SPH GADGET (Springel 2005) code. The oldest GADGET 2 version was used for Set 2 simulations, already presented by Dolag et al. (2009), while Set 1 was completed using the newest version 3. The difference between the two versions resides mainly in the different algorithm adopted for domain decomposition. Both versions of the code use segments of the space-filling Peano–Hilbert curve to decide the particles to be assigned to different processors. Unlike GADGET 2, the newest GADGET 3 version allows each processor also to be assigned disjoined segments of the Peano–Hilbert curve. This turns out to yield a substantial improvement of the workload balance assigned to the different processors, especially for simulations like those presented here in which the computation cost is largely concentrated within quite a small fraction of the physical volume of the computational domain.

We add here below a brief description for each of the physical models adopted within our simulations.

(i) NR-SV (non-radiative, standard viscosity): non-radiative runs, using the standard reference scheme for artificial viscosity implemented in GADGET. This prescription is based on the formulation of artificial viscosity originally presented by Monaghan (1997), also including a viscosity limiter as proposed by Balsara (1995) and Steinmetz (1996).

(ii) NR-RV (non radiative, reduced viscosity): non-radiative runs, using reduced time-dependent viscosity, as originally proposed by

Morris & Monaghan (1997) and implemented in GADGET by Dolag et al. (2005). In this scheme, artificial viscosity decays away from shock regions, thus allowing a higher degree of turbulence in the velocity field to develop.

(iii) CSF (cooling star formation and feedback): runs including radiative cooling for a zero-metallicity plasma, including heating/cooling from a spatially uniform and evolving UV background (Haardt & Madau 1996). Gas particles above a given threshold density are treated as multiphase, so as to provide a subresolution description of the interstellar medium, according to the model described by Springel & Hernquist (2003). Within each multiphase gas particle, a cold and a hot phase coexist in pressure equilibrium, with the cold phase providing the reservoir of star formation. Kinetic feedback is implemented by giving some SN II energy to gas particles in the form of kinetic energy, thus mimicking galactic ejecta powered by SN explosions. In these runs, galactic winds have a mass upload proportional to the local star-formation rate. We use $v_{\rm w} = 340\,{\rm km\,s^{-1}}$ for the wind velocity, which corresponds to assuming half of energy released by SN II being converted to kinetic energy for a Salpeter IMF (Salpeter 1955).

(iv) CSF-C (csf and thermal conduction): the same as the CSF runs, but also including the effect of thermal conduction as described by Jubelgas, Springel & Dolag (2004) and Dolag et al. (2004). The conduction efficiency is assumed to have a value of 1/3 of the Spitzer conductivity.

(v) CSF-M-W (csf, metals and galactic winds): radiative runs with star formation described through the same multiphase model as the CSF runs. In addition, CSF-M-W runs also include a description of metal production from chemical enrichment contributed by SN II, SN Ia and AGB stars, as described by Tornatore et al. (2007). Stars of different mass, distributed according to a Salpeter IMF (Salpeter 1955), release metals over the time-scale determined by the corresponding mass-dependent lifetimes (taken from Padovani & Matteucci 1993). The metallicity dependence of radiative cooling is included by using the cooling tables of Sutherland & Dopita (1993). In these runs, the velocity of galactic ejecta is assumed to be $v_{\rm w} = 500\,{\rm km\,s^{-1}}$, thus corresponding to a more efficient SN feedback that in the CSF runs.

(vi) CSF-M-NW (csf, metals and no winds): the same as CSF-M-W but with no winds, i.e. by excluding the effect of kinetic feedback from galactic winds.

(vii) CSF-M-AGN (csf, metals and AGN): the same as the CSF-M-W runs, but replacing SN feedback in the form of galactic winds, with the effect of AGN feedback triggered by gas accretion on to supermassive black holes (BH). Details about this feedback model are discussed in Fabjan et al. (2010), while we summarize here only the main points. The scheme is a slight modification of the model introduced by Springel, Di Matteo & Hernquist (2005), where BH are represented by sink particles initially seeded in resolved dark matter (DM) haloes. These particles increase their mass by gas accretion and merging with other BH particles. Eddington-limited Bondi accretion produces a radiated energy that corresponds to a fraction $\epsilon_r = 0.1$ of the rest-mass energy of the accreted gas. A fraction $\epsilon_{\rm f}$ of this radiated energy is thermally coupled to the surrounding gas. We use $\epsilon_{\rm f} = 0.05$ for this feedback efficiency, which increases to $\epsilon_{\rm f} = 0.2$ whenever accretion enters in the quiescent 'radio' mode and takes place at a rate smaller than one-hundreth of the Eddington limit (Sijacki & Springel 2006; Fabjan et al. 2010).

We remark here that galaxy clusters in Set 2 were simulated with all the presented baryon physics models, while simulations of Set 1 clusters were performed with NR-SV and CSF-M-W physics only.

The diversity and heterogeneity of the description of physical processes determining the evolution of the ICM is not meant to provide a systematic study of the parameter space describing the ICM physics. However, quantifying the variation of the scaling relations between mass proxies and true cluster mass for each of the models will allow us to assess the robustness of mass proxies against the uncertainties in the description of the ICM physics.

2.2 Initial conditions and simulation sets

Our analysis is based on two sets of simulations of galaxy clusters. The two sets, while having similar mass and force resolution, are quite different in a number of aspects and allow us to perform complementary tests on the robustness of mass proxies. The extensive statistics of Set 1 clusters allows us to calibrate with precision the slope and scatter of the scaling relations along with their evolution, while the variety of different physical processes of Set 2 are used to assess the robustness of mass proxies against the uncertainties in the description of the ICM physics.

We provide in the following a more technical description of these two sets of simulations.

2.2.1 Set 1

This set is based on simulations of 29 Lagrangian regions, extracted around as many clusters, identified within low-resolution N-body cosmological simulations. We provide here a short description of these initial conditions, while a more detailed presentation will be provided in a forthcoming paper (Bonafede et al. 2011). The parent DM simulation follows 1024^3 DM particles within a box having a comoving side of $1\,h^{-1}$ Gpc. The cosmological model assumed is a flat ΛCDM one, with $\Omega_{\rm m} = 0.24$ for the matter density parameter, $\Omega_{\rm bar} = 0.04$ for the contribution of baryons, $H_0 = 72\,{\rm km\,s^{-1}\,Mpc^{-1}}$ for the present-day Hubble constant, $n_{\rm s} = 0.96$ for the primordial spectral index and $\sigma_8 = 0.8$ for the normalization of the power spectrum in terms of the root-mean-square (r.m.s.) fluctuation level at $z = 0$ within a top-hat sphere of $8\,h^{-1}$ Mpc radius. With the above choice of parameters, this cosmological model is consistent with the cosmic microwave background (CMB) *WMAP*-7 constraints (Komatsu et al. 2011). The selected Lagrangian regions have been chosen so that 24 of them are centred around the 24 most massive clusters found in the cosmological volume, all having virial[2] mass $M_{\rm vir} \gtrsim 10^{15}\,h^{-1}\,{\rm M_\odot}$. A further five regions have been chosen around clusters in the mass range $M_{\rm vir} \simeq (1-7) \times 10^{14}\,h^{-1}\,{\rm M_\odot}$.

Within each Lagrangian region we increased mass resolution and added the relevant high-frequency modes of the power spectrum, following the zoomed initial condition (ZIC) technique (Tormen, Bouchet & White 1997). Initial conditions for hydrodynamic simulations have been generated by splitting each particle within the high-resolution region into a DM and a gas particle, having mass ratio such as to reproduce the cosmic baryon fraction. Outside high-resolution regions the resolution is progressively degraded, so as to save computational time while preserving a correct description of the large-scale tidal field. We generated initial conditions at different, progressively increasing, resolutions. For the hydrodynamic

[2] Here we define the virial mass $M_{\rm vir}$ as the mass contained within the radius encompassing the overdensity of virialization, as predicted by the spherical collapse model (e.g. Eke, Cole & Frenk 1996).

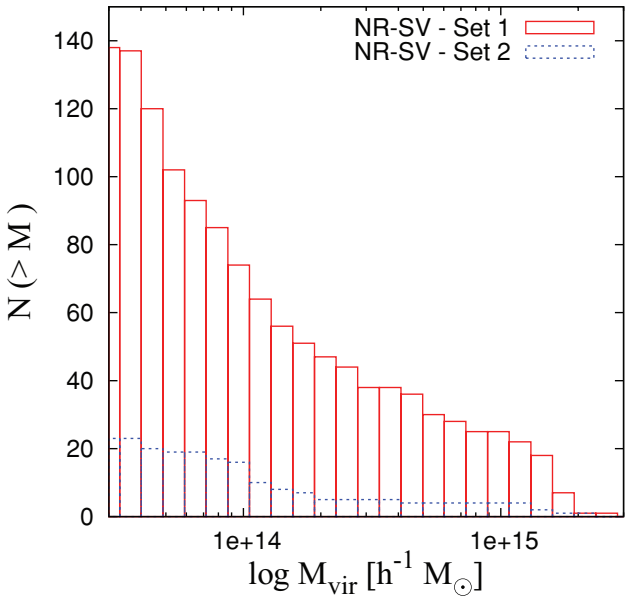

Figure 1. The cumulative distributions of virial masses for clusters in Set 1 (red solid histogram) and in Set 2 (blue dashed histogram). We only count 'clean' clusters, for which no contaminant low-resolution DM particles are found within their corresponding virial radii.

simulations presented here the mass of each DM particle in the high-resolution region is $m_{\rm DM} \simeq 8.47 \times 10^8\, h^{-1}\,{\rm M}_\odot$, with $m_{\rm gas} \simeq 1.53 \times 10^8\, h^{-1}\,{\rm M}_\odot$ for the initial mass of gas particles. Using an iterative procedure, we have shaped each high-resolution Lagrangian region in such a way that no low-resolution particle contaminates the central 'zoomed in' halo at $z = 0$ at least out to 5 virial radii of the central cluster. This implies that each region is sufficiently large to contain more than one interesting cluster with no 'contaminants' out to at least one virial radius. In total, we find $\simeq$140 clusters with $M_{500} \geq 5 \times 10^{13}\, h^{-1}\,{\rm M}_\odot$, out of which about 40 have $M_{\rm vir} > 5 \times 10^{14}\, h^{-1}\,{\rm M}_\odot$ and 30 have $M_{\rm vir} > 10^{15}\, h^{-1}\,{\rm M}_\odot$. We show in Fig. 1 the cumulative mass distribution for this set of simulated clusters.

Simulations have been carried out using a Plummer-equivalent softening length for the computation of the gravitational force in the high-resolution region, which is fixed to $\epsilon = 5\, h^{-1}$ kpc in physical units at redshift $z < 2$, while being kept fixed in comoving units at higher redshift. As for the computation of hydrodynamic forces, we assume the SPH smoothing length reaches a minimum allowed value of 0.5ϵ.

Clusters from this set have been simulated using the NR-SV and CSF-M-W models. The NR-SV set is the only one simulated with GADGET 3 code.

2.2.2 *Set 2*

This set is based on nine Lagrangian regions selected from a parent DM-only cosmological box with a size of $479\, h^{-1}$ Mpc Yoshida, Sheth & Diaferio (2001). The cosmological model assumed is ΛCDM with $\Omega_M = 0.3$ for the matter density, $h = 0.7$ for the Hubble parameter, $\Omega_{\rm bar} = 0.039$ for the baryon density parameter and $\sigma_8 = 0.9$ for the normalization of the power spectrum. We refer to Dolag et al. (2009) for a more detailed description of this set of clusters. Briefly, this set includes overall 18 clusters with $M_{\rm vir} > 5 \times 10^{13}\, h^{-1}\,{\rm M}_\odot$, out of which only four have $M_{\rm vir} > 10^{15}\, h^{-1}\,{\rm M}_\odot$. The mass distribution of these clusters is shown in Fig. 1.

Mass resolution is quite close to that of Set 1 ($m_{\rm DM} \simeq 1.9 \times 10^8\, h^{-1}\,{\rm M}_\odot$ and $m_{\rm gas} \simeq 2.8 \times 10^7\, h^{-1}\,{\rm M}_\odot$ for DM and gas particles respectively), also with the same choices for the size of the gravitational softening scale and the minimum allowed value of the SPH smoothing length. Clusters from this set have been simulated with GADGET 2 using all seven different models described above for the description of the baryon physics.

3 RESULTS AND DISCUSSION

3.1 Mass proxies

The mass proxies that we consider in our analysis are the mass-weighted temperature $T_{\rm mw}$, the gas mass $M_{\rm gas}$ and the product of gas mass and temperature, $Y_X = M_{\rm gas} \times T_{\rm mw}$. All these quantities are computed within the fiducial radius R_{500}, which typically corresponds to the outermost radius at which scaling relations from observational data analysis are provided (Vikhlinin et al. 2009a; Sun et al. 2009; Pratt et al. 2009; Maughan 2007). With the purpose of reproducing the procedure of observational analyses, we exclude the central regions $R < 0.15R_{500}$ in the computation of the temperature. The reason for this choice in the analysis of real clusters is that temperature profiles show a rather high degree of diversity in such central regions depending on their degree of 'cool-coreness' (Vikhlinin et al. 2006; Pratt et al. 2007; Leccardi & Molendi 2008). Excluding such regions suppresses the scatter in the scaling relation involving temperature (see Pratt et al. 2009, and references therein). Furthermore, it places us in the regime in which simulations are in closer agreement with observations (Borgani et al. 2004). The choice of the radial interval in which to compute mass proxies represents our only attempt to introduce 'observational effects' in our analysis. Indeed, in this paper (Paper I) we prefer to analyse the intrinsic performance of the three above mass proxies in detail, i.e. neglecting any possible observational bias, which will be addressed in Paper II (Rasia et al., in preparation). We want to stress that in this analysis (i) we estimate all quantities in three dimensions (i.e. neglecting projection effects); (ii) unless otherwise stated, we use the mass-weighted definition of temperature; (iii) we do not remove gas clumps at relatively low temperature when we compute both temperature and gas mass.

The simplest description of scaling relations between galaxy cluster mass and X-ray observables is that provided by the self-similar model originally proposed by Kaiser (1986). According to this model, the thermodynamical properties of the ICM are determined only by the action of gravity, under the assumption of virial equilibrium and spherical symmetry (e.g. Voit 2005b, for a review). Within this model, cluster total mass is the only parameter that determines all the thermodynamical properties of the hot intracluster gas. Accordingly, the cluster gas mass within the radius R_Δ is proportional to the total mass computed within the same radius,

$$M_{{\rm tot},\Delta} = C_{M_{\rm g}} M_{{\rm gas},\Delta}\,, \qquad (1)$$

with constant of proportionality $C_{M_{\rm g}}$ being independent of redshift. The total mass is related to the temperature according to

$$M_{{\rm tot},\Delta} = E(z)^{-1} C_T T_\Delta^{3/2}\,, \qquad (2)$$

where $E(z) = H(z)/H_0$ defines the evolution of the Hubble parameter. Therefore, as defined in the paper by Kravtsov et al. (2006), the self-similar scaling of Y_X with cluster mass is given by

$$M_{{\rm tot},\Delta} = C_{Y_X} E(z)^{-2/5} Y_{X,\Delta}^{3/5}\,. \qquad (3)$$

In the above relations involving ICM temperature, the mass-averaged $T_{\rm mw}$ should be used, since it is more directly related to

the total ICM thermal content. As such, this is the quantity relevant for the predictions of the self-similar model, rather than the spectroscopic temperature which is more affected by the complexity of the ICM thermal structure.

In the following we analyse the scaling relations for simulated clusters with masses $M_{\rm vir} > 5 \times 10^{13}\,h^{-1}\,{\rm M}_\odot$ at five different redshifts: $z = 0$, 0.25, 0.5, 0.8 and 1. To fit the scaling relation between total mass $M_{\rm tot,500}$ and a given observable mass proxy X_{500}, we use a power law:

$$M_{\rm tot,500} = C_X \left(\frac{X_{500}}{X_0}\right)^{\alpha_X} . \quad (4)$$

Following the work by Kravtsov et al. (2006), the normalization factor X_0 was fixed to $2 \times 10^{13}\,{\rm M}_\odot$, 3 keV and $4 \times 10^{13}\,{\rm keV\,M}_\odot$ for $M_{\rm gas}$, $T_{\rm mw}$ and Y_X, respectively. We also perform fits by fixing the slope α_X to the self-similar values $\alpha_{\rm SS} = 1.0$, 1.5 and 0.6 for M_{500}–$M_{\rm gas}$, M_{500}–$T_{\rm mw}$ and M_{500}–$Y_{\rm X}$, respectively.

The values of the slope α_X and normalization C_X are obtained by performing a best fit to the log–log relation by using the least-squares Marquardt–Levenberg algorithm (Press et al. 1992). This algorithm calculates at each iteration the sum of the squared differences with a new set of parameter values; the Marquardt–Levenberg algorithm selects the parameter values for the next iteration. The process continues until a preset criterion is met: either the fit has converged (the relative change in the residuals is less than 10^{-6}) or it reaches a preset iteration count limit. The intrinsic scatter in natural logarithm of the total mass $\ln M_{\rm tot}$ around each best-fitting scaling relation is computed as the quadratic difference between the single cluster data and the relation fitted on the whole cluster set.

3.2 Scaling relations at $z = 0$

In this section we discuss the behaviour of the M_{500}–$M_{\rm gas}$, M_{500}–$T_{\rm mw}$ and M_{500}–$Y_{\rm X}$ relations for the radiative (CSF-M-W) and non-radiative (NR-SV) simulations at $z = 0$ for the simulated clusters of Set 1.

In Fig. 2 we show the relations between the total cluster mass M_{500} and $M_{\rm gas}$ (left panel), $T_{\rm mw}$ (middle panel) and Y_X (right panel). Besides the results of the analysis for radiative (CSF-M-W in red circles) and non-radiative (NR-SV in blue squares) simulations, we plot the best-fitting relations obtained when the slope is fixed to the corresponding self-similar values, shown with red long-dashed and blue short-dashed lines for the CSF-M-W and NR-SV simulations, respectively.

Galaxy clusters in non-radiative simulations show a behaviour close to the self-similar one for the three relations studied. Indeed, when we consider the slope as free parameter the new best fits (not shown) over all NR-SV clusters return values consistent with $\alpha_{\rm SS}$, namely $\alpha = 0.981 \pm 0.004$ for $M_{\rm gas}$, $\alpha = 1.517 \pm 0.012$ for $T_{\rm mw}$ and $\alpha = 0.597 \pm 0.03$ $Y_{\rm X}$, respectively. Results of the fitting relations are reported in Tables 1, 2, and 3 for $Y_{\rm X}$, $M_{\rm gas}$, and $T_{\rm mw}$, respectively. The agreement with the self-similar scaling for $T_{\rm mw}$ was also found by Stanek et al. (2010) for clusters extracted from the non-radiative version of the millenium gas simulations (MGS).

When radiative cooling and star formation are included in CSF-M-W simulations, the average quantities change, thus modifying the slope and normalization of the scaling relations. The CSF-M-W clusters (red circles in Fig. 2) deviate from the self-similar scaling relation for both $M_{\rm gas}$ and $T_{\rm mw}$. As for the M_{500}–$M_{\rm gas}$ scaling, the best-fitting relation has a shallower slope. This is due to the fact that for radiative simulations the conversion of baryons into stars is relatively more efficient in lower mass clusters, thus corresponding to a lower mass fraction of gas left in the hot diffuse phase (Borgani et al. 2004; Kravtsov, Nagai & Vikhlinin 2005; Fabjan et al. 2010). For the M_{500}–$T_{\rm mw}$ relation, the results for the radiative runs are characterized by a slope steeper than the self-similar one, with $\alpha = 1.615 \pm 0.016$. In this case, the effect of including radiative physics is to increase the temperature of the ICM by a larger amount in less massive systems. Indeed, the more efficient cooling in lower-mass systems causes a relatively stronger adiabatic compression of gas in central core regions, as a consequence of the lack of pressure support. As a result, temperature profiles in radiative simulations of clusters are relatively steeper in less massive systems (see also Borgani et al. 2004).

The deviations with respect to self-similarity that we detect in the M_{500}–$M_{\rm gas}$ and M_{500}–$T_{\rm mw}$ relations for radiative simulations are

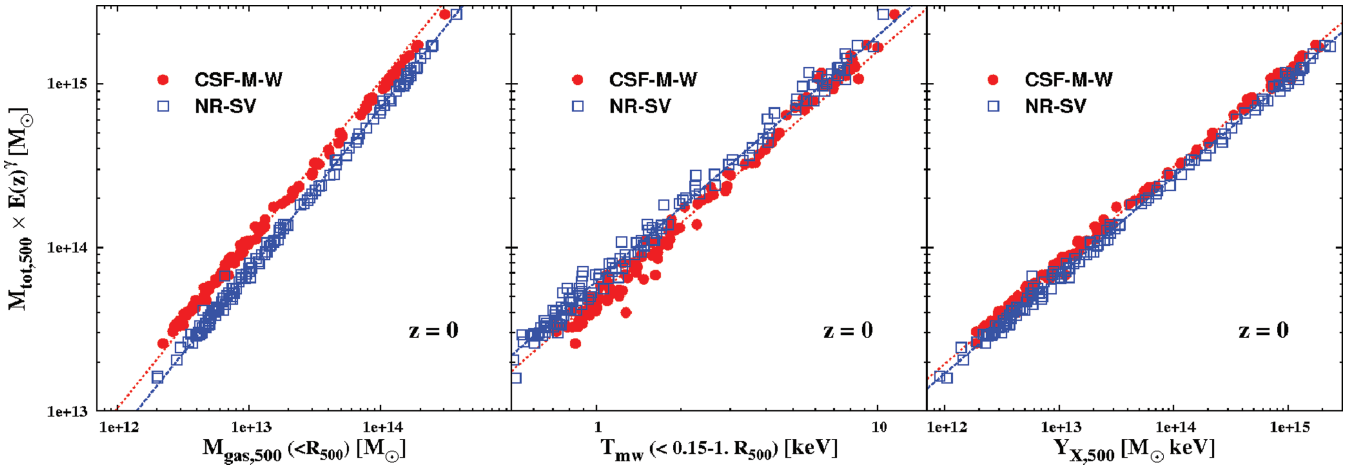

Figure 2. Scaling relations at $z = 0$ between the total mass computed within R_{500} and three mass proxies: $M_{\rm gas}$, $T_{\rm mw}$ and $Y_{\rm X}$. The evolution of the relation is scaled accordingly, with $\gamma = 0$, 1 and 2/5, respectively. On each figure we plot the results for non-radiative (blue open squares) and radiative (red filled circles) runs for clusters in Set 1 with $M_{\rm vir} > 5 \times 10^{13}\,h^{-1}\,{\rm M}_\odot$. The short-dashed (red) and dashed (blue) lines are the best-fitting relations of radiative and non-radiative cluster simulations respectively, with slopes fixed to the self-similar value. Left panel: scaling with $M_{\rm gas}$; central panel: scaling with mass-weighted temperature, $T_{\rm mw}$; right panel: scaling with $Y_{\rm X}$. The values of $T_{\rm mw}$ appearing in the central panel and entering in the computation of $Y_{\rm X}$ in the right panel are computed within the radial range $(0.15–1)R_{500}$.

Table 1. Fitting parameters for the M_{500}–$Y_{\rm X}$ relation for the simulated clusters of Set 1. Results are obtained through a log–log linear regression using equation (4), with $Y_{\rm X,0} = 4 \times 10^{13}$ keV $\rm M_\odot$. Reported errors in the fitting parameters correspond to 1σ standard deviation in the linear fit. Also reported are the values of r.m.s. scatter in $M_{\rm tot,500}$ and in $Y_{\rm X,500}$ around the fitting relations. Different columns refer to results at different redshifts. The first two lines report results for non-radiative (NR-SV) simulations, the other two instead the results for radiative (CSF-M-W) simulations. For each simulation we report first the best-fitting parameters and below the results when the slope of the scaling relation is fixed at the value predicted by the self-similar model.

	$z = 0$	$z = 0.25$	$z = 0.50$	$z = 0.80$	$z = 1$
			NR-SV best-fitting parameters		
α_{Y_X}	0.597 ± 0.003	0.599 ± 0.003	0.604 ± 0.003	0.601 ± 0.004	0.604 ± 0.005
$\log C_{Y_X}$	14.190 ± 0.002	14.188 ± 0.002	14.189 ± 0.002	14.177 ± 0.003	14.185 ± 0.004
$\sigma_{\ln M}$	0.064	0.067	0.067	0.070	0.073
$\sigma_{\ln Y_X}$	0.107	0.111	0.111	0.117	0.122
			NR-SV self-similar scaling ($\alpha_{Y_X} = 0.6$)		
$\log C_{Y_X}$	14.191 ± 0.002	14.188 ± 0.002	14.187 ± 0.002	14.177 ± 0.002	14.183 ± 0.003
$\sigma_{\ln M}$	0.064	0.067	0.067	0.070	0.074
$\sigma_{\ln Y_X}$	0.107	0.111	0.112	0.117	0.123
			CSF-M-W best-fitting parameters		
α_{Y_X}	0.591 ± 0.003	0.590 ± 0.002	0.596 ± 0.003	0.591 ± 0.003	0.596 ± 0.005
$\log C_{Y_X}$	14.249 ± 0.002	14.247 ± 0.002	14.250 ± 0.002	14.248 ± 0.003	14.252 ± 0.004
$\sigma_{\ln M}$	0.050	0.051	0.054	0.061	0.076
$\sigma_{\ln Y_X}$	0.084	0.086	0.091	0.104	0.128
			CSF-M-W self-similar scaling ($\alpha_{Y_X} = 0.6$)		
$\log C_{Y_X}$	14.250 ± 0.003	14.250 ± 0.002	14.252 ± 0.002	14.253 ± 0.002	14.255 ± 0.002
$\sigma_{\ln M}$	0.052	0.054	0.055	0.063	0.076
$\sigma_{\ln Y_X}$	0.087	0.089	0.091	0.104	0.127

Table 2. The same as Table 1, but for the M_{500}–$M_{\rm gas}$ relation. In this case we use $M_{\rm gas,0} = 2 \times 10^{13}$ $\rm M_\odot$ for the normalization factor in equation (4).

	$z = 0$	$z = 0.25$	$z = 0.50$	$z = 0.80$	$z = 1$
			NR-SV best-fitting parameters		
$\alpha_{M_{\rm gas}}$	0.981 ± 0.004	0.983 ± 0.003	0.991 ± 0.004	0.991 ± 0.004	0.999 ± 0.005
$\log C_{M_{\rm gas}}$	14.154 ± 0.002	14.142 ± 0.002	14.136 ± 0.002	14.130 ± 0.002	14.127 ± 0.002
$\sigma_{\ln M}$	0.055	0.048	0.047	0.041	0.040
$\sigma_{\ln M_{\rm gas}}$	0.056	0.049	0.047	0.041	0.040
			NR-SV self-similar scaling ($\alpha_{Y_X} = 1$)		
$\log C_{M_{\rm gas}}$	14.155 ± 0.002	14.144 ± 0.002	14.138 ± 0.002	14.132 ± 0.001	14.128 ± 0.001
$\sigma_{\ln M}$	0.061	0.052	0.048	0.042	0.040
$\sigma_{\ln M_{\rm gas}}$	0.061	0.052	0.048	0.042	0.040
			CSF-M-W best-fitting parameters		
$\alpha_{M_{\rm gas}}$	0.929 ± 0.003	0.926 ± 0.003	0.929 ± 0.003	0.924 ± 0.004	0.933 ± 0.005
$\log C_{M_{\rm gas}}$	14.310 ± 0.002	14.298 ± 0.002	14.291 ± 0.002	14.285 ± 0.002	14.288 ± 0.003
$\sigma_{\ln M}$	0.039	0.043	0.039	0.046	0.047
$\sigma_{\ln M_{\rm gas}}$	0.042	0.047	0.042	0.050	0.050
			CSF-M-W self-similar scaling ($\alpha_{Y_X} = 1$)		
$\log C_{M_{\rm gas}}$	14.317 ± 0.004	14.320 ± 0.003	14.320 ± 0.002	14.320 ± 0.002	14.322 ± 0.002
$\sigma_{\ln M}$	0.090	0.092	0.078	0.080	0.068
$\sigma_{\ln M_{\rm gas}}$	0.090	0.092	0.078	0.080	0.068

not present in the M_{500}–$Y_{\rm X}$ relation. In fact the best-fitting slope of cluster data is 0.591 ± 0.003, close to the value of $\alpha_{\rm SS} = 0.6$ predicted by the self-similar model. As apparent from the right panel of Fig. 2, including cooling, star formation and SN feedback in the CSF-M-W runs has only a modest effect on the M_{500}–$Y_{\rm X}$ scaling. The reason for this is that the $Y_{\rm X}$ mass proxy provides a measure of the total thermal content of the ICM. Since this total thermal content is dominated by the mechanism of gravitational accretion of baryons within the DM-dominated potential wells of clusters, it is not surprising that the scaling of $Y_{\rm X}$ with total cluster

Table 3. The same as Table 1, but for the M_{500}–$T_{\rm mw}$ relation. In this case we use $T_{\rm mw,0} = 3$ keV for the normalization factor in equation (4).

	$z = 0$	$z = 0.25$	$z = 0.50$	$z = 0.80$	$z = 1$
			NR-SV best-fitting parameters		
$\alpha_{T_{\rm mw}}$	1.517 ± 0.012	1.515 ± 0.016	1.534 ± 0.016	1.498 ± 0.021	1.495 ± 0.027
$\log C_{T_{\rm mw}}$	14.513 ± 0.006	14.524 ± 0.007	14.535 ± 0.007	14.507 ± 0.009	14.530 ± 0.010
$\sigma_{\ln M}$	0.120	0.145	0.134	0.146	0.150
$\sigma_{\ln T_{\rm mw}}$	0.079	0.096	0.087	0.098	0.101
			NR-SV self-similar scaling ($\alpha_{Y_X} = 1.5$)		
$\log C_{T_{\rm mw}}$	14.508 ± 0.005	14.519 ± 0.005	14.524 ± 0.004	14.508 ± 0.005	14.531 ± 0.005
$\sigma_{\ln M}$	0.120	0.145	0.135	0.146	0.150
$\sigma_{\ln T_{\rm mw}}$	0.080	0.097	0.090	0.098	0.100
			CSF-M-W best-fitting parameters		
$\alpha_{T_{\rm mw}}$	1.615 ± 0.016	1.614 ± 0.013	1.640 ± 0.017	1.608 ± 0.019	1.596 ± 0.028
$\log C_{T_{\rm mw}}$	14.427 ± 0.006	14.436 ± 0.005	14.450 ± 0.006	14.445 ± 0.006	14.444 ± 0.009
$\sigma_{\ln M}$	0.111	0.106	0.127	0.132	0.163
$\sigma_{\ln T_{\rm mw}}$	0.069	0.066	0.077	0.082	0.102
			CSF-M-W self-similar scaling ($\alpha_{Y_X} = 1.5$)		
$\log C_{T_{\rm mw}}$	14.413 ± 0.007	14.410 ± 0.005	14.414 ± 0.005	14.417 ± 0.004	14.419 ± 0.005
$\sigma_{\ln M}$	0.134	0.127	0.147	0.142	0.168
$\sigma_{\ln T_{\rm mw}}$	0.089	0.085	0.098	0.094	0.112

mass is very close to the self-similar prediction and that its value, at a fixed cluster mass, is weakly sensitive to the inclusion of non-radiative physics. This is even more true when, as in our analysis, we exclude central cluster regions, which are more affected by radiative cooling.

Besides the stability of the scaling relations against variations of the ICM physics, another useful quantity to judge the robustness of mass proxies is the intrinsic scatter around the best-fitting relations. In fact, the intrinsic scatter and its distribution are also an important quantities to look at when deciding which mass proxy is the best one for cosmological applications of galaxy clusters (Lima & Hu 2005; Shaw, Holder & Dudley 2010). Looking at Fig. 2, we note that the mass-weighted temperature is the proxy with the largest scatter, both for CSF-M-W and NR-SV runs. To display the scatter of each relation graphically we plot in Fig. 3 the distribution of residuals with respect to the best-fitting relation, in log mass. In all panels the distribution of the residuals is close to a log-normal one. The intrinsic mass scatter in the residuals of the M– $M_{\rm gas}$ relation is $\sigma_{\ln M} \simeq 0.039$ and 0.055 for the CSF-M-W and NR-SV simulations, respectively (see also Table 2). The largest scatter is obtained for the mass-weighted temperature $T_{\rm mw}$, reaching values of $\sigma_{\ln M} \simeq 0.11$ and 0.12 for non-radiative and radiative simulations, respectively, thus similar to the result found by Stanek et al. (2010) for their non-radiative simulations (see also Table 3). For the $Y_{\rm X}$ proxy, the intrinsic scatter in mass is $\sigma_{\ln M} \simeq 0.050$ and 0.064 for CSF-M-W and NR-SV simulations, respectively.

Therefore, while the $Y_{\rm X}$ mass proxy is found to have the scaling with mass closest to the self-similar behaviour, almost independently of the inclusion of radiative physics and SN feedback, the proxy having the lowest scatter against mass is $M_{\rm gas}$. This result is in line with that obtained by Stanek et al. (2010) from the analysis of clusters simulated with SPH, both with non-radiative physics and including cooling plus the effect of a phenomenological pre-heating. Similarly to our analysis, Stanek et al. did not attempt to include observational effects in their analysis, while they analysed scaling relations at a larger radius, R_{200} instead of R_{500} as in our analysis.

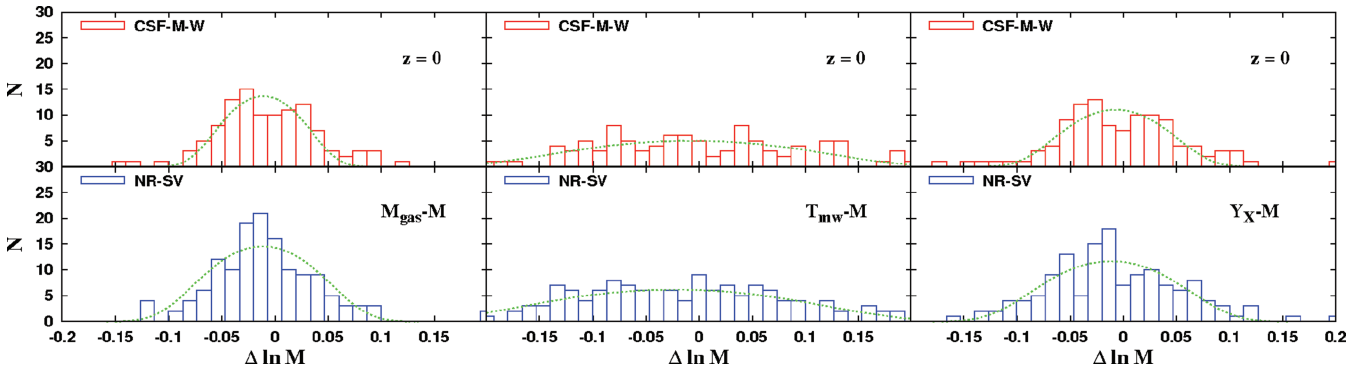

Figure 3. Distributions of the residuals in log mass in the scaling relations at $z = 0$ between mass proxies and $M_{\rm tot,500}$, for non-radiative (upper/red histograms) and radiative (lower/blue histograms) runs of simlated clusters from Set 1. Residuals are computed with respect to the relation that fits the simulated cluster data best. Left panel: scaling with $M_{\rm gas}$; central panel: scaling with mass-weighted temperature, $T_{\rm mw}$; right panel: scaling with $Y_{\rm X}$. Dotted curves (green) show the Gaussian distribution with the same variance as the distribution of residuals in mass (as reported in Tables 1, 2 and 3).

We also note that indications for a lower scatter in the M_{500}–$M_{\rm gas}$ relation than in the M_{500}–$Y_{\rm X}$ relation have also been reported by Okabe et al. (2010) from the analysis of observational data. Their analysis was based on *XMM–Newton* data for the measurement of X-ray mass proxies and on weak lensing data for the measurement of total cluster masses. These results are, however, at variance with the original result by Kravtsov et al. (2006), who instead found $Y_{\rm X}$ to be the lowest-scatter mass proxy from their analysis of cluster simulations based on the ART adaptive-mesh refinement code. In their analysis, Kravtsov et al. showed that the residuals ΔT in the M_{500}–$T_{\rm mw}$ relation and $\Delta M_{\rm gas}$ in the M_{500}–$M_{\rm gas}$ relation anticorrelate in their radiative simulations when computed with respect to the best-fitting self-similar relation, thus justifying the smaller scatter found in the M–$Y_{\rm X}$ scaling. Indeed the latter can be computed as $\sigma_Y^2 = \sigma_{T_{\rm mw}}^2 + \sigma_{M_{\rm gas}}^2 + 2C_{T,M}\sigma_T\sigma_{M_{\rm gas}}$, where $C_{T,M}$ is the correlation coefficient and σ denotes the scatter values of temperature and gas mass (Stanek et al. 2010).

In order to look at the behaviour of such residuals in our simulations, we plot in Fig. 4 the residuals in $\ln T_{\rm mw}$ versus the residuals in $\ln M_{\rm gas}$ determined at fixed total mass M_{500}. The residuals are computed with respect to the best-fitting relations computed without imposing the self-similar slope. Evaluating Pearson's correlation coefficient $r_{\rm P}$ for the residuals, we found them to be uncorrelated. We find $r_{\rm P} = 0.24$ for the NR-SV distribution (left panel) and $r_{\rm P} = 0.11$ for the CSF-M-W one (right panel). The presence of a weak positive correlation explains why the scatter in Y_X is, if anything, slightly larger than that in $M_{\rm gas}$. In order to reproduce more closely the procedure followed by Kravtsov et al. (2006), we then repeated the analysis by computing the residuals with respect to the best-fitting self-similar relation. The results in this case are shown in Fig. 5. For the non-radiative runs (left panel) we find that $\Delta\ln T_{\rm mw}$ and $\Delta\ln M_{\rm gas}$ are again consistent with being uncorrelated for the NR-SV simulations, with $r_{\rm P} = 0.14$. However, such scatters show a more evident sign of anticorrelation for the CSF-M-W simulations, $r_{\rm P} = -0.53$.

In order to make more clear the reason for the anticorrelation in the residuals computed with respect to the self-similar best-fitting relation for the radiative runs, we show with different symbols in Figs 4 and 5 the points corresponding to clusters within different mass ranges: the cyan triangles show the most massive objects with $M_{500} > 5 \times 10^{14}\,{\rm M}_\odot$, the green points refer to groups with $M_{500} < 10^{14}\,{\rm M}_\odot$, while red squares represent the intermediate clusters. The only panel showing anticorrelation, the right panel of Fig. 5, also shows a clear trend with cluster mass. Anticorrelation for CSF-M-W clusters is actually a direct result of the offset of scaling relations in temperature and gas mass with respect to the expected self-similar ones. As already discussed, in the radiative runs the two relations show an opposite behaviour with respect to self-similarity: M–$M_{\rm gas}$ and M–$T_{\rm mw}$ are correspondingly shallower and steeper than the self-similar scaling. This means that massive clusters in CSF-M-W simulations do have higher gas masses and lower temperatures. On the other side, in low-mass clusters the amount of gas is lower and temperatures are higher than expected. Therefore, in this case the presence of an anticorrelation is only a spurious effect of imposing the self-similar slopes on the best-fitting scaling relations used to compute such residuals. Clearly, in comparing our results with those by Kravtsov et al. (2006) one should remember that their analysis attempted to include observational effects in the estimate of the temperature and the gas mass. The analysis presented here, instead, is aimed at quantifying the intrinsic performances of the different mass proxies, i.e. before convolving with the effect of measuring temperature from X-ray spectra and gas mass from a projected map of X-ray surface brightness. Quite likely, including such observational effects could affect both scaling relations and the intrinsic scatter around them through the distribution of the residuals. We will address in detail these issues in a forthcoming paper (Rasia et al., in preparation).

In summary, the results presented in this section have shown that (i) $M_{\rm gas}$ has an intrinsic scatter against cluster mass slightly smaller than $Y_{\rm X}$, while both proxies have a significantly lower scatter than

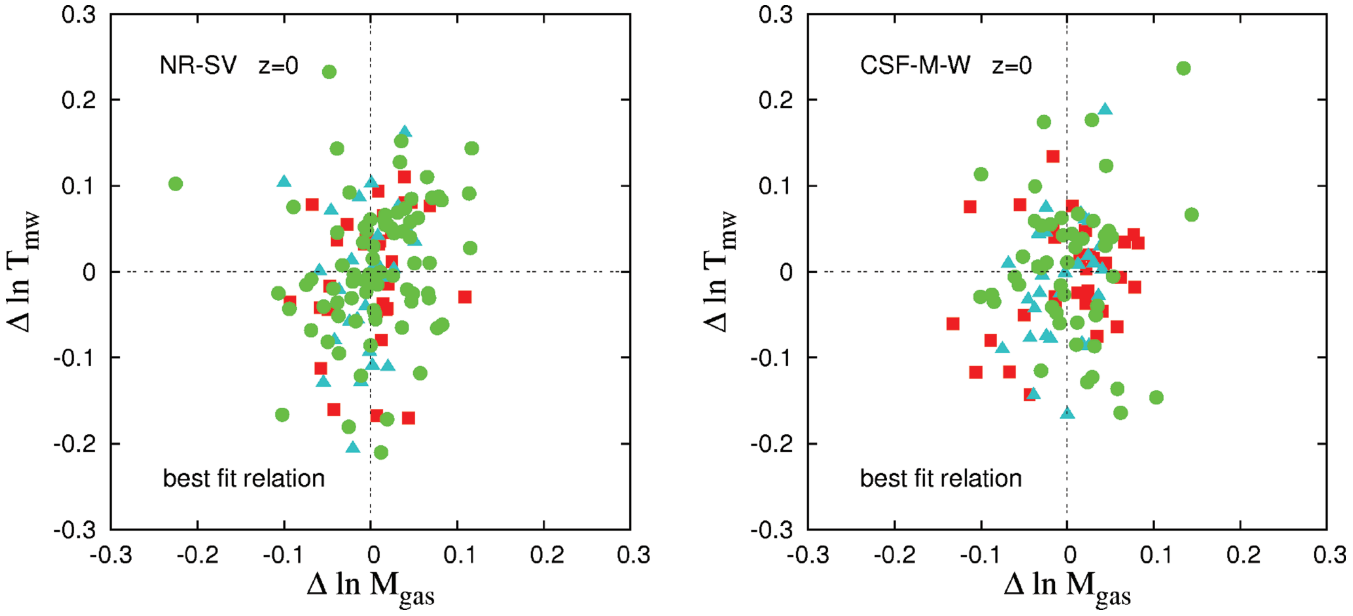

Figure 4. The residuals in $\ln T_{\rm mw}$ versus the residuals in $\ln M_{\rm gas}$ at fixed values of M_{500} for clusters at $z = 0$. Residuals are evaluated with respect to the best-fitting M_{500}–$T_{\rm mw}$ and M_{500}–$M_{\rm gas}$ relations at $z = 0$. Left and right panels are respectively for non-radiative (NR-SV) and radiative (CSF-M-W) simulations of clusters of Set 1. Different symbols and colours correspond to different ranges in M_{500}: triangles (cyan) for $M_{500} > 5 \times 10^{14}\,{\rm M}_\odot$; squares (red) for $10^{14} < M_{500} < 5 \times 10^{14}\,{\rm M}_\odot$; circles (green) for $5 \times 10^{13} < M_{500} < 10^{14}\,{\rm M}_\odot$.

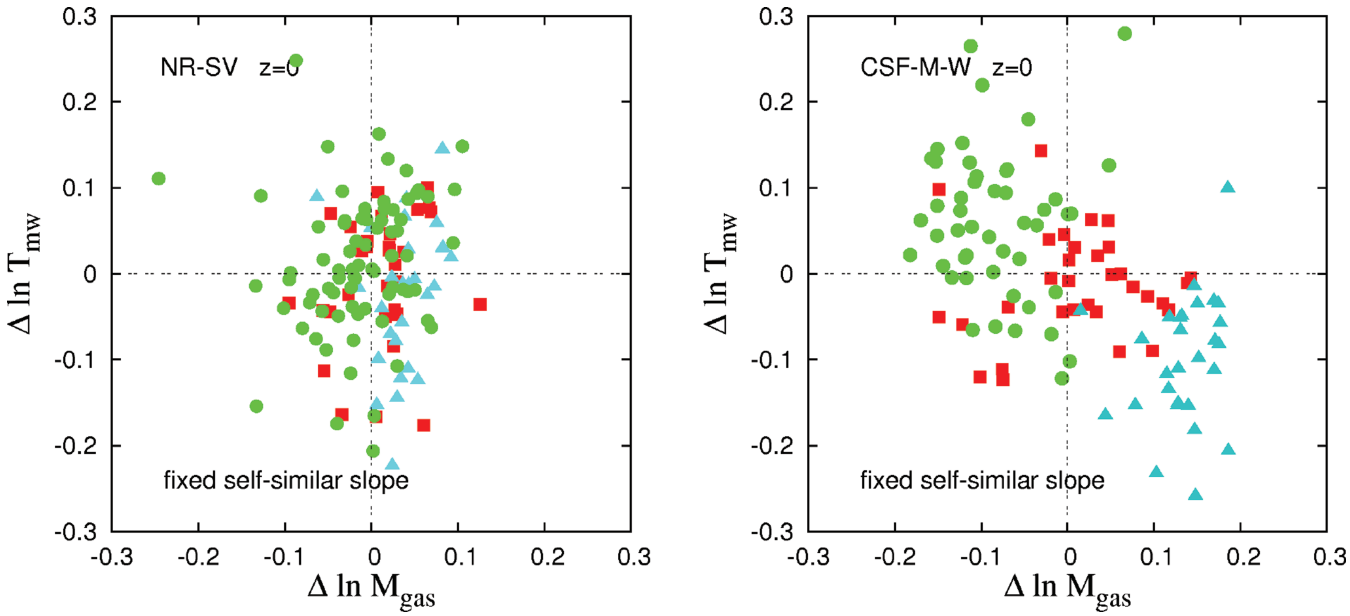

Figure 5. The same as in Fig. 4 but for deviations with respect to the best-fitting relation obtained by fixing the slopes to the self-similar values. Symbols and colours have the same meaning as in Fig. 4.

$T_{\rm mw}$, and (ii) $Y_{\rm X}$ is the proxy for which the scaling against mass has the weakest dependence on the inclusion of radiative physics and the slope of which is closest to the prediction of the self-similar model. The latter result is in line with the expectation that $Y_{\rm X}$ is a measure of the total thermal energy content of the ICM, which is mostly determined by gravitational processes once central cluster regions are excluded from the analysis. Moreover, we found that residuals in $T_{\rm mw}$ and $M_{\rm gas}$ with respect to the best-fitting relations are uncorrelated, independently of the adopted simulation, while anticorrelation seen in radiative simulations is as a result of the offset of M_{500}–$T_{\rm mw}$ and M_{500}–$M_{\rm gas}$ relations with respect to the expected self-similar ones.

3.3 Stability against changing ICM physics

In order to investigate further the sensitivity of the different mass proxies to the physics included in the simulation, in this section we use results from the analysis of the Set 2 simulated clusters. As already discussed in Section 2, this set is characterized by a much smaller number of simulated clusters than Set 1, but includes 7 different prescriptions to describe the baryonic physics.

As first test we verify that simulated clusters from Set 1 and Set 2 do produce consistent results when simulated with the same physics (despite the fact that they are based on somewhat different cosmological models). We show in Fig. 6 results from the

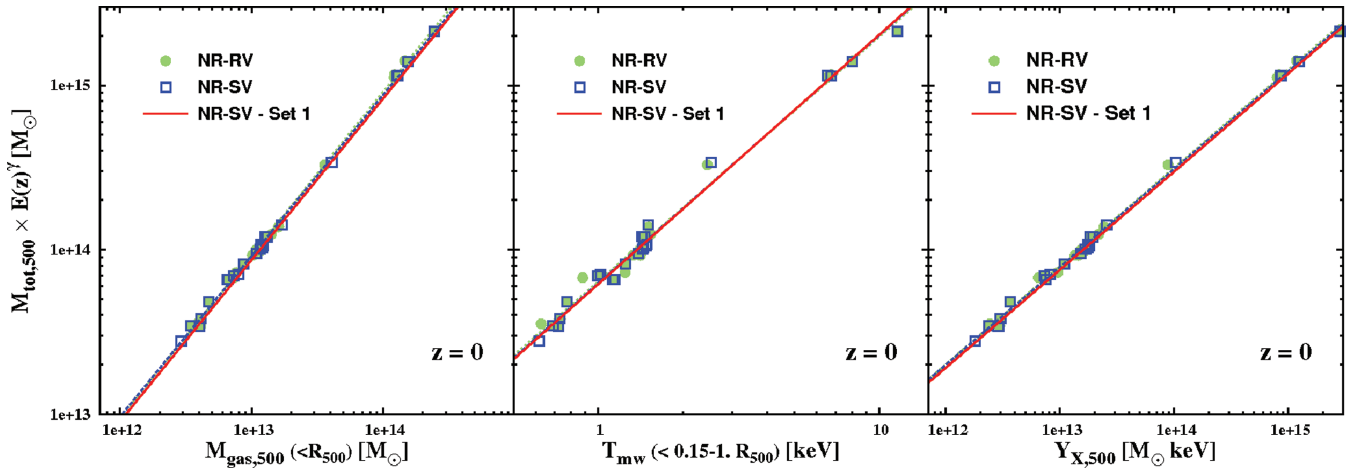

Figure 6. Scaling relations at $z = 0$ between the total mass and three mass proxies ($Y_{\rm X}$ and $M_{\rm gas}$ computed inside R_{500}, $T_{\rm mw}$ evaluated extracting the central $0.15\,R_{500}$). The evolution of the relation is scaled accordingly, with $\gamma = 2/5, 0$ and 1, respectively. Best fits of non-radiative Set 2 simulations are represented by long-dashed (green) and short-dashed (blue) lines (NR-RV and NR-SV respectively), compared with the best fit of the Set 1 NR-SV clusters shown with a continuous line (red). For this comparison we scaled the results of $M_{\rm gas}$ and $T_{\rm mw}$ obtained for clusters of Set 1 simulations to the baryon fraction of Set 2.

non-radiative runs (NR-SV and NR-RV) of Set 2 and compare them with the best-fitting relation for the NR-SV version of Set 1 (continuous line). In performing this comparison, we should account for the different values of the baryon fraction assumed in the two simulation sets (see Section 2.1). To account for this, we scaled $M_{\rm gas}$ and $Y_{\rm X}$ for the Set 1 simulation NR-SV by multiplying them by the ratio of the two baryon fractions: $f_{\rm b,Set1}/f_{\rm b,Set2} \simeq 1.2$. From this plot we note that results for the NR-SV versions of Set 1 and Set 2 agree very well with each other. Furthermore, we also note that the best fitting relations for the NR-SV and NR-RV simulations of clusters of Set 2 are also extremely similar. As shown by Dolag et al. (2005), using the time-dependent reduced viscosity scheme has the effect of increasing turbulent motions in the ICM (see also Valdarnini 2011). Therefore, the stability of results against variations in the adopted viscosity scheme (still within SPH hydrodynamics) implies that non-thermal pressure support associated with turbulent motions has only a very modest impact on the overall gas mass and thermal content in our simulated clusters.

As for radiative simulations, we verified the effect of changing feedback efficiency and including thermal conduction. All such processes are expected to change the gas distribution and the temperature structure of the ICM and, therefore, potentially to impact on the scaling relations of mass proxies against total cluster mass. We plot in Fig. 7 such scaling relations obtained for the different radiative runs CSF, CSF-C, CSF-M-NW, CSF-M-W and CSF-M-AGN, along with their best-fitting relations.

The relations involving gas mass and temperature (left and central panels, respectively) show significant dependence on the physical processes included in the simulations, especially for relatively low-mass systems. In general, while the effect of including thermal conduction is quite small, the separation between simulations with and without AGN feedback is more evident. Indeed, AGN feedback has the effect of removing a significant amount of gas from the innermost regions (Fabjan et al. 2010), thus inducing a decrease of $M_{\rm gas}$, which is more pronounced for galaxy groups than for rich clusters. This effect can be observed in the central panel of Fig. 7, where the slope of the best-fitting relation for AGN simulations is $\alpha = 0.81$, thus significantly flatter than the $\alpha = 1$ self-similar scaling. The effect of AGNs is not only to remove a large amount of gas from the centre of galaxy groups but also to heat up the ICM in the central regions of such systems. This can be seen in the M_{500}–$T_{\rm mw}$ relation shown in the central panel, where the resulting slope of the relation is $\alpha = 1.73$, again quite different from the $\alpha = 1.5$ self-similar value. Simulations including the effect of galactic winds, namely CSF, CSF-C and CSF-M-W, do have a slope closer to the self-similar one for both the M_{500}–$M_{\rm gas}$ ($\alpha \simeq 0.9$) and M_{500}–$T_{\rm mw}$ ($\alpha \simeq 1.5$–1.6) relation. The clusters simulated without feedback have an intermediate behaviour for both relations. Similarly to the results already seen for simulations of Set 1, M_{500}–$T_{\rm mw}$ is the scaling relation characterized by the largest scatter.

On the other hand, the M_{500}–$Y_{\rm X}$ relation (right panel in Fig. 7) is confirmed to be the one with the weakest sensitivity to the baryon physics included in the simulation. To further emphasize the different sensitivity that different mass proxies have to the ICM physics, we plot in Fig. 8 the logarithm of the normalization $\log C$ and the slope α of all the best-fitting scaling relations for the seven different physical models simulated for the clusters of Set 2. $T_{\rm mw}$ and $M_{\rm gas}$ show the largest discrepancies in $\log C$, varying from 14.2 to 14.5 in both relations. The $Y_{\rm X}$ proxy instead has a more stable behaviour, with values around 14.25–14.35. Radiative runs also show a consistent off-set from the self-similar slopes in the case of $M_{\rm gas}$ and $T_{\rm mw}$, while the slope of the M_{500}–$Y_{\rm X}$ relation is in good agreement with the self-similar value of $\alpha = 0.6$ for all the models considered. A maximum deviation of $\simeq$11 per cent is only present in the case of CSF-M-AGN feedback.

In summary, in this section we have shown that the $Y_{\rm X}$ mass proxy is the most robust one against changing the physical processes that determine the thermodynamical properties of the ICM and its scaling with total cluster mass has a slope that is always very close to that predicted by the self-similar model.

3.4 Evolution of scaling relations

For mass proxies to be used in cosmological applications of galaxy clusters, one has to calibrate precisely not only the normalization, slope and scatter of the scaling relations with total mass for low-redshift systems but also the evolution with redshift. Redshift evolution is especially important when considering distant clusters located at the highest redshifts, $z \gtrsim 1$, where they have been secured to date in statistically complete X-ray surveys. Indeed, as we

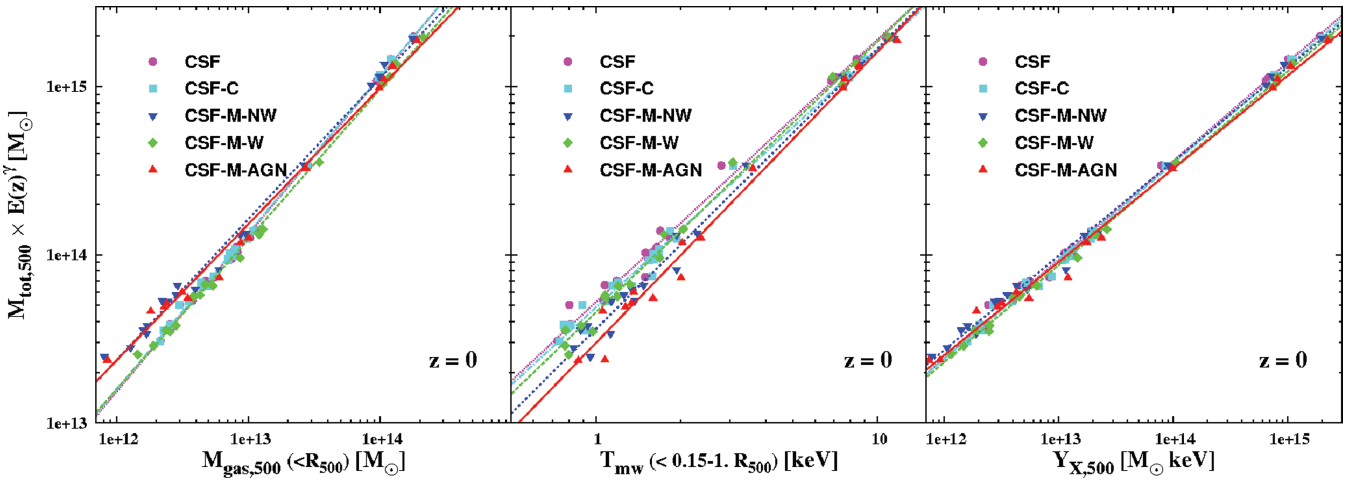

Figure 7. Effect of different physics models on scaling relations between total mass and $Y_{\rm X}$, $M_{\rm gas}$ and $T_{\rm mw}$ at $z = 0$ for the radiative simulations of Set 1. The evolution of the relation is scaled accordingly, with $\gamma = 2/5$, 0 and 1, respectively. For each simulated physics we plot cluster data with dots (purple, CSF), squares (cyan, CSF-C), downward-pointing triangles (blue, CSF-M-NW), diamonds (green, CSF-M-W) and upward-pointing triangles (red, CSF-M-AGN). For clarity, data points are overplotted with the best-fitting relation for each of the five physics simulations, using the same colour coding as for the points.

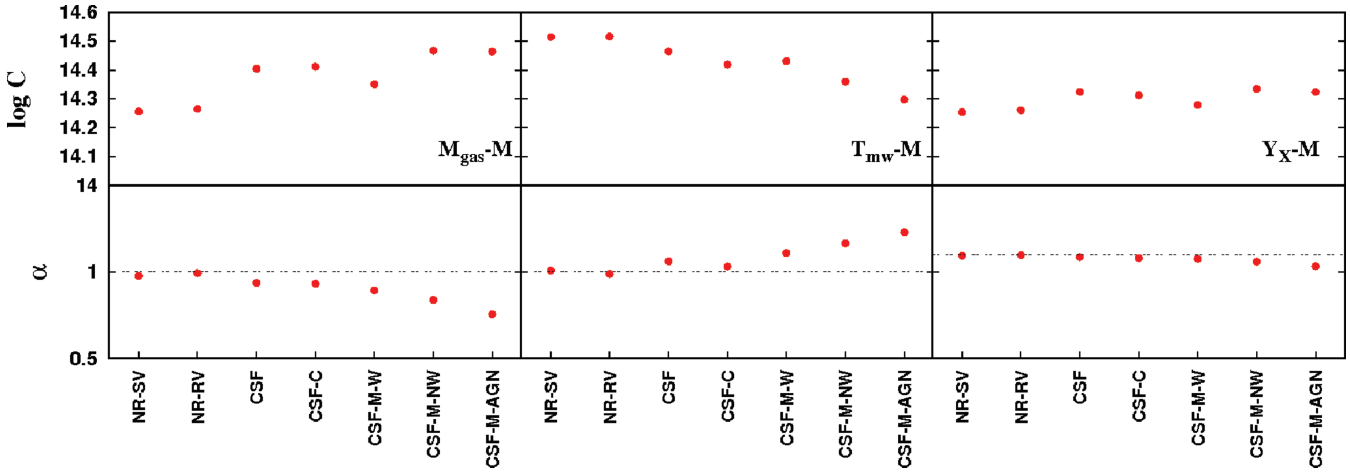

Figure 8. Dependence of the best-fitting slope α (lower panels) and normalization C (upper panels) of the scaling relations of the three mass proxies against total cluster mass. Results for for M_{500}–$M_{\rm gas}$, M_{500}–$T_{\rm mw}$ and M_{500}–$Y_{\rm X}$ are shown in the left, central and right panels, respectively. In the lower panel, the horizontal dashed lines mark the values of the slope of the scaling relations predicted by the self-similar model.

approach the epoch of cluster assembly one expects clusters to be characterized by major mergers, which may impact significantly on the shaping of such scaling relations. This issue is of crucial importance if we want to constrain cosmological parameters by using upcoming and future large cluster surveys, based on the next generation of wide-field X-ray telescopes (Borgani et al. 2011; Cappelluti et al. 2011).

In this section we will address the evolution of scaling relations and their intrinsic scatter. For an accurate study of the evolution of scaling relations, we resort to the large statistical data base of clusters for Set 1 simulations. All simulated clusters are analysed at five redshifts: $z = 0, 0.25, 0.5, 0.8$ and 1. After measuring the normalization C and slope α of the scaling relations at each redshift, their redshift evolution is described through the relations

$$\log C(z) = \log C_0(z) + \beta_1 (1+z)\,,$$
$$\alpha(z) = \alpha_0 + \beta_2 (1+z)\,. \qquad (5)$$

Similarly to Short et al. (2010), who studied the evolution of scaling relations from millennium simulations, we take the redshift dependence of $C_0(z)$ to be that predicted by the self-similar model. Therefore, we expect $\beta_1 = 0$ for self-similar evolution of the normalization.

We list in Table 4 the values of the parameters that describe, through equation (5), the evolution of the scaling relations between the three mass proxies $M_{\rm gas}$, $T_{\rm mw}$ and $Y_{\rm X}$ and the cluster total mass. Moreover, we plot in Fig. 9 the redshift dependence of the normalization (after accounting for self-similar evolution; upper panels) and slope (lower panels) of these scaling relations. The $M_{\rm gas}$ proxy has a very mild negative evolution with redshift ($\beta_1 < 0$) for both radiative and non-radiative simulations. The slope is confirmed to be very close to the self-similar value for non-radiative simulations at all redshifts, with negligible evolution of its value, while being shallower for the radiative simulations. For the mass-weighted temperature, a slightly positive evolution is detected for the CSF simulations, while the evolution is very close to self-similar for NR simulations.

Quite interestingly, the M_{500}–$Y_{\rm X}$ scaling relation is the one with both the weakest sensitivity to the ICM physics at all redshifts and the smallest deviations from the self-similar predictions regarding the evolution of the normalization and the value of the slope. These results confirm once again the robustness of the $Y_{\rm X}$ mass proxy

Table 4. Best-fitting values for the parameters determining the evolution of normalization C and slope α of the scaling relations of $M_{\rm gas}$, $T_{\rm mw}$ and $Y_{\rm X}$ against M_{500}, as described by equation (5), over the redshift range $0 \le z \le 1$. For each relation the values obtained for both CSF-M-W and NR-SV simulations are reported. The reported uncertainties correspond to 1σ uncertainties in the linear regression.

	$\log C_0$	β_1	α_0	β_2
		$M_{\rm gas} - M_{500}$		
CSF-M-W	14.307 ± 0.003	-0.079 ± 0.015	0.927 ± 0.003	0.005 ± 0.017
NR-SV	14.152 ± 0.001	-0.086 ± 0.007	0.979 ± 0.002	0.057 ± 0.011
		$T_{\rm mw} - M_{500}$		
CSF-M-W	14.430 ± 0.005	0.059 ± 0.025	1.622 ± 0.014	-0.047 ± 0.070
NR-SV	14.518 ± 0.011	0.020 ± 0.054	1.524 ± 0.012	-0.075 ± 0.061
		$Y_{\rm X} - M_{500}$		
CSF-M-W	14.248 ± 0.002	0.007 ± 0.008	0.591 ± 0.002	0.011 ± 0.012
NR-SV	14.191 ± 0.004	-0.030 ± 0.019	0.597 ± 0.002	0.023 ± 0.009

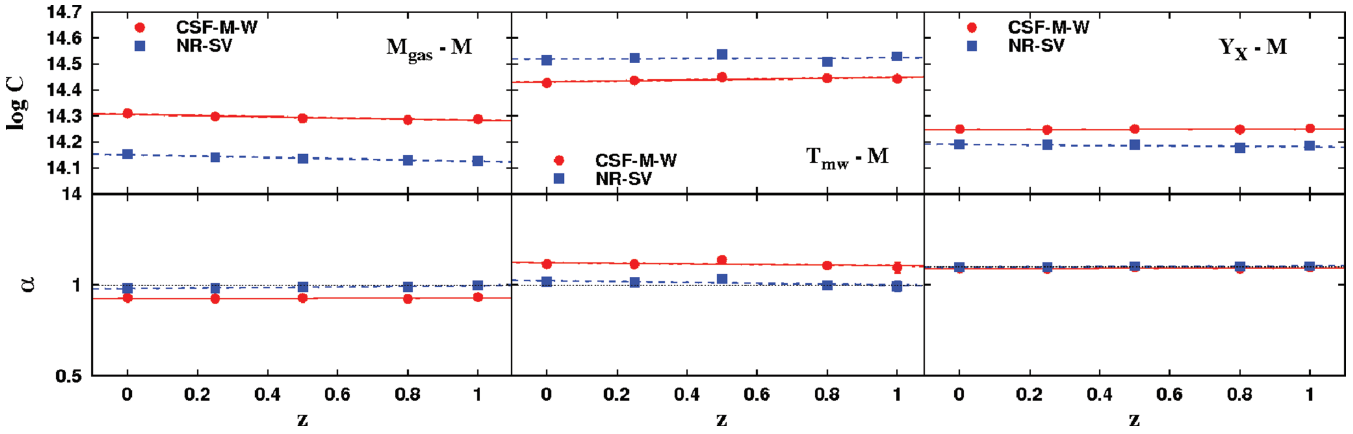

Figure 9. Redshift dependence of the best-fitting parameters that define the scaling relations between mass proxies and $M_{\rm tot,500}$. Left panel: scaling with $Y_{\rm X,500}$; central panel: scaling with $M_{\rm gas,500}$; right panel: scaling with mass-weighted temperature, $T_{\rm mw}$ (see equation 5). Results for CSF-M-W and NR-SV simulations are plotted with circles (red) and squares (blue), respectively. For each point we also plot the error bars corresponding to the 1σ uncertainty from the log–log linear regression, the size of which is smaller than the size of the points. The horizontal dotted lines in the lower panels mark the values of slope α predicted by self-similar scaling. For the amplitude C, its redshift dependence marks the degree of deviation from the evolution predicted by the self-similar model.

against variations in the physics of the ICM over the whole redshift range considered. They further confirm that since this mass proxy provides a measure of the ICM total thermal energy content, it can be reliably described on grounds of the predictions of the self-similar model. Indeed, this model is based on the assumption that gravitational mechanisms determine the thermal content of the ICM, an assumption that is expected not to be violated by radiative and feedback processes, once we exclude the core regions of galaxy clusters.

A further important aspect that characterizes the behaviour of the three analysed mass proxies at different redshifts is the evolution of their intrinsic scatter. We plot the evolution of this intrinsic scatter in Fig. 10 for both CSF (red circles) and NR (blue squares) simulated clusters. The intrinsic scatter for the M_{500}–$M_{\rm gas}$ relation, shown in the left panel of Fig. 10, is remarkably low for both simulations, with a slight positive (negative) evolution for the radiative (non-radiative) simulations. In general, the intrinsic scatter in mass, $\sigma_{\ln M}$, for $M_{\rm gas}$ varies in the narrow range 4–5 per cent at all considered redshifts. CSF clusters instead show a mild decrease, with a constant 4 per cent scatter below $z < 0.5$. Such small values are expected, since gas mass is not sensitive to cluster mergers, which are expected to play an increasingly important role at higher redshift. The middle panel of Fig. 10 shows instead the evolution of intrinsic scatter for the M_{500}–$T_{\rm mw}$ relation. In this case we note that the intrinsic scatter is larger and shows clear sign of positive evolution for both radiative and non-radiative simulations, with an increase from $\sigma_{\ln M} \gtrsim 10$ per cent at $z = 0$ to $\gtrsim$15 per cent at $z = 1$. The increase of the scatter in the M_{500}–$T_{\rm mw}$ relation agrees with the expectation that temperature is more sensitive than gas mass to the presence of substructures in the ICM, which are expected to be more prominent at high redshift, when cluster mergers are more frequent. The M_{500}–$Y_{\rm X}$ scaling relation has a positive evolution that is driven by the positive evolution of the scatter in the M_{500}–$T_{\rm mw}$ relation (right panel of Fig. 10). In general the intrinsic scatter increases from $\sigma_{\ln M} \simeq$ 5–6 per cent at low redshift to $\lesssim$8 per cent at $z = 1$.

The analysis presented in this section confirms that gas mass is the mass proxy behaving best as regards the intrinsic scatter in its scaling relation with total mass, in terms of both value and stability with redshift.

An important caveat is not to overinterpret the results presented here with regard to the fact that the small values of intrinsic scatter for all mass proxies have been obtained by neglecting observational

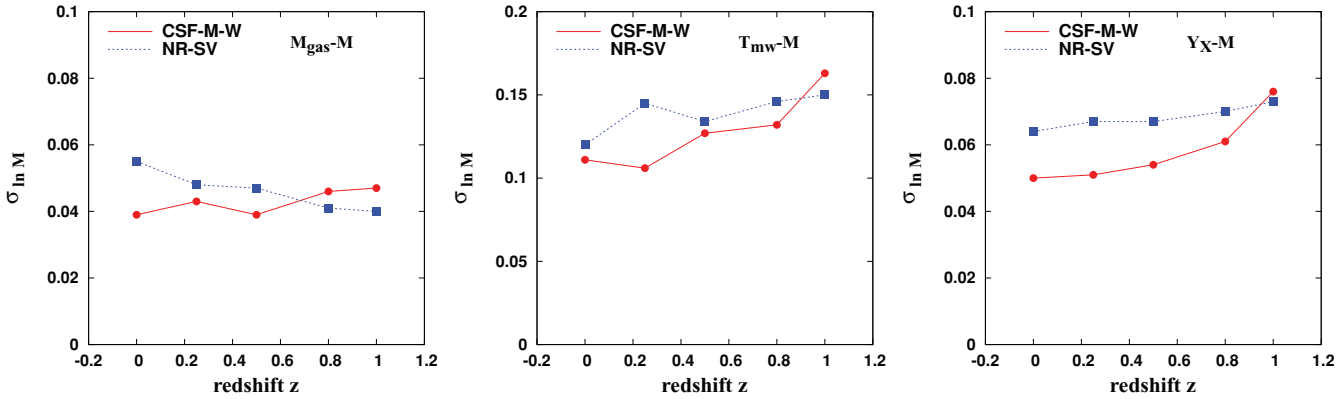

Figure 10. Redshift evolution of the intrinsic scatter $\sigma_{\ln M}$ in the scaling relations for simulated clusters of Set 1: results are plotted with circles (red) for CSF-M-W simulations and squares (blue) for NR-SV simulations. Left, middle and right panels show results for $M_{\rm tot,500}$–$M_{\rm gas}$, $M_{\rm tot,500}$–Y_X and $M_{\rm tot,500}$–$T_{\rm mw}$, respectively. Note that the y-axis range in the middle panel is twice that for the other two panels.

effects in the measurement of mass proxies. Such observational effects are in general expected to introduce intrinsic scatter. A typical example is provided by the presence of substructures that are not resolved in realistic observational conditions. The contribution of the X-ray emissivity from the high-density, low-temperature substructures impacts both on the estimate of the gas mass from the X-ray surface-brightness profile and on the spectroscopic measurement of temperature (Mazzotta et al. 2004; Vikhlinin 2006). In this way, observational determinations of gas mass and temperature will have a larger scatter in their scaling relation with cluster mass than their mass-weighted counterpart.

4 CONCLUSIONS

Galaxy clusters are powerful tools for cosmological studies, since the evolution of their mass function constrains the normalization of the power spectrum, the density parameter of dark matter and dark energy, as well as the dark-energy equation of state, through the linear growth rate of density perturbations. When observed in the X-ray band, their high emissivity allows clusters to be detected out to high redshifts, $z \sim 1.5$. However, to exploit fully the potential of galaxy clusters as tracers of cosmic evolution, it is necessary to understand in detail the relation between mass proxies, based on easy-to-measure X-ray observables, and total cluster mass.

In this paper we focused on the study of the $M_{\rm gas}$, $T_{\rm mw}$ and $Y_{\rm X}$ mass proxies and the effect that different physical mechanisms have on the mass–observable relations. The aim of this analysis was to answer, through simulations, three questions. (1) Which mass proxy is least sensitive to our uncertain knowledge of the physical processes determining the thermodynamical structure of the ICM? (2) To what extent do such mass proxies follow the predictions of the self-similar model regarding the shape of scaling relations and their redshift evolution? (3) How large is the intrinsic scatter in these scaling relations and how does it evolve with redshift?

To answer these questions, we used galaxy clusters simulated with SPH using GADGET. We combined two different sets of simulations: Set 1, composed of more than 100 clusters with mass above $5 \times 10^{13} h^{-1} {\rm M}_{\odot}$, was used for its high statistics, to calibrate scaling relations and study their scatter and redshift evolution. Set 2, containing many fewer clusters simulated with seven different different physics schemes, was instead used to study the effects of (i) thermal conduction, (ii) artificial viscosity, (iii) cooling and star formation, (iv) galactic winds and (v) AGN feedback.

The main results of our analysis can be summarized as follows.

(1) In non-radiative simulations, the relations between cluster total mass and the three considered mass proxies closely follow the self-similar prediction.

(2) In radiative simulations, the M_{500}–$M_{\rm gas}$ and M_{500}–$T_{\rm mw}$ scaling relations show opposite deviations from self-similarity. The net result is a sort of compensating effect in the M_{500}–$Y_{\rm X}$ relation, with a nearly self-similar slope.

(3) The M_{500}–$Y_{\rm X}$ relation is the most stable against change of the physical processes included in the simulations, with its slope and evolution always being very close to the predictions of the self-similar model, which is based on the assumption that gravity alone drives the ICM thermodynamics. Indeed, the $Y_{\rm X}$ proxy is by definition a measure of the total thermal content of the ICM, which is dominated by the gravitational process of gas accretion.

(4) M_{500}–$M_{\rm gas}$ is found to be the scaling relation with the lowest scatter in mass, 4–6 per cent. Moreover, the amount of scatter in this case is almost constant with redshift, independently of the simulated physics.

(5) The scatter in the M_{500}–$Y_{\rm X}$ relation is slightly larger that for the M_{500}–$M_{\rm gas}$ relation; its intrinsic scatter grows with redshift as a consequence of the increase of merging events and presence of substructure in the ICM.

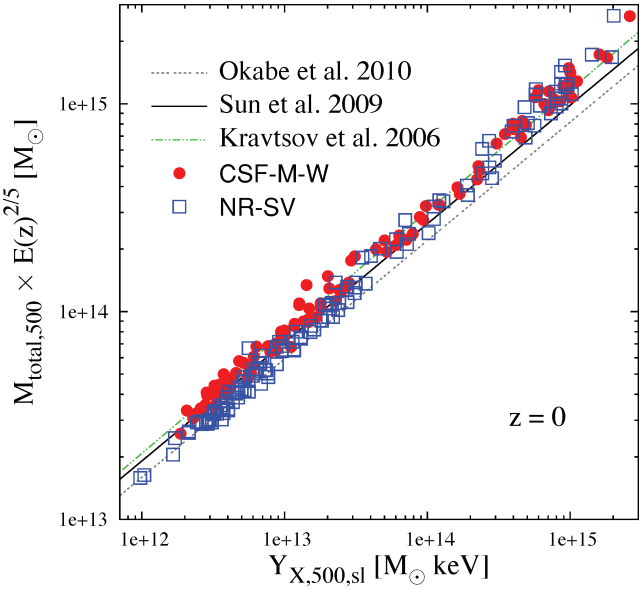

Figure 11. Comparison between the $M_{\rm tot,500}$–$Y_{\rm X,500,sl}$ relations for radiative simulations (CSF-M-W with circles, red) and non-radiative simulations (NR-SV with squares, blue) of clusters of Set 1 at $z = 0$, and results presented in the literature from simulations and observational data. For this comparison, we resorted to the spectroscopic-like definition of temperature (Mazzotta et al. 2004; Vikhlinin 2006) for the computation of $Y_{\rm X,sl}$ in our simulations. The dot-dashed (green) line corresponds to the best-fitting relation from the radiative simulation by Kravtsov et al. (2006). The continuous (black) line is the best-fitting relation found by Sun et al. (2009) from the analysis of *Chandra* data of clusters and groups. The long-dashed (grey) line is the best fit found by Okabe et al. (2010) for the relation between Y_X computed from *XMM–Newton* data and weak lensing masses from Subaru observations.

As already mentioned in previous sections, the analysis discussed in this paper differs in spirit from that presented by Kravtsov et al. (2006), who instead presented results based on the inclusion of projection effects and spectroscopic estimates of the ICM temperature. In order to have a first assessment of the effect of carrying out a more observationally oriented analysis, we also computed the $Y_{\rm X}$ mass proxy using a spectroscopic-like definition of temperature, $T_{\rm sl}$. To this purpose, we followed the procedure described by Vikhlinin (2006), which generalizes the analytic formula originally introduced by Mazzotta et al. (2004) to include relatively cold clusters with temperature below 3 keV.[3] We plot in Fig. 11 the scaling relation between total mass and $Y_{\rm X,500,sl} = M_{\rm gas} \times T_{\rm sl}$ for the radiative and non-radiative versions of the clusters of

[3] We use the algorithm proposed by Vikhlinin (2006), which resorts to precomputed tables of some parameters of the observed spectra as a function of temperature. Tables were generated with the code that is publicly available at http://hea-www.harvard.edu/~alexey/mixT. The tables were created by fixing $N_{\rm H} = 5 \times 10^{20}$ for the galactic hydrogen column density, setting solar abundances at the values of Grevesse & Sauval (1998), using the *Chandra* ACIS-S CCD response function and a photon energy range of 0.7–10 keV.

Set 1. As expected, the scatter in this case is larger than when adopting the mass-weighted definition of temperature: it increases from $\sigma_{\ln M} = 0.06$ to 0.10 and from $\sigma_{\ln M} = 0.05$ to 0.08 for the NR-SV and CSF-M-W simulations, respectively. Moreover a slight deviation from self-similarity is also observed for non-radiative runs, with $\alpha = 0.64$, while the slope for radiative runs, $\alpha = 0.60$, agrees with the self-similar value. In the same figure we also compare our results with those presented in literature, both from simulations (Kravtsov et al. 2006) and from observational data (Sun et al. 2009; Okabe et al. 2010). Our results are in a good agreement, although some discrepancy is seen at the high-mass end of clusters and for NR-SV galaxy groups.

Clearly, a more detailed analysis of how observational effects will affect the scaling relations measured from our simulated cluster sets requires the use of dedicated software, such as X-ray Map Simulator (X-MAS: Gardini et al. 2004; Rasia et al. 2005, 2008) to extract mock images and spectra from simulations and to reduce data using the same procedure followed for observational data (Rasia et al., in preparation).

ACKNOWLEDGMENTS

We are greatly indebted to Volker Springel for providing us with the non-public version of GADGET. We acknowledge useful discussions with Gus Evrard, Andrey Kravtsov and Chris Miller. This work has been partially supported by PRIN-MIUR grant 'The Cosmic Cycle of Baryons', ASI–AAE and ASI–COFIS grants, the INFN–PD51 grant and PRIN-INAF 2009 grant "Towards an italian network for computational cosmology". DF acknowledges support by the European Union and Ministry of Higher Education, Science and Technology of Slovenia. ER acknowledges the Michigan Society of Fellows. KD acknowledges the financial support of the 'HPC-Europa Transnational Access program' and the hospitality of CINECA and the Department of Physics of the University of Trieste. DF, SB and ER acknowledge the hospitality of the Sesto Center for Astrophysics (SCfA), where part of the work was carried out. Simulations have been carried out at the CINECA Supercomputing Center (Bologna), with CPU time assigned thanks to an INAF–CINECA grant and an agreement between CINECA and the University of Trieste.

REFERENCES

Ameglio S., Borgani S., Pierpaoli E., Dolag K., Ettori S., Morandi A., 2009, MNRAS, 394, 479
Arnaud M., Pratt G. W., Piffaretti R., Boehringer H., Croston J. H., Pointecouteau E., 2010, A&A, 517, A92
Balsara D. S., 1995, J. Comput. Phys., 121, 357
Bartelmann M., Steinmetz M., 1996, MNRAS, 283, 431
Bonafede A., Dolag K., Stasyszyn F., Murante G., Borgani S., 2011, MNRAS, in press (arXiv:1107.0968)
Borgani S., Kravtsov A., 2009, ASL, in press (arXiv:0906.4370)
Borgani S. et al., 2001, ApJ, 561, 13
Borgani S. et al., 2004, MNRAS, 348, 1078
Borgani S., Rosati P., Sartoris B., Tozzi P., Giacconi R., WFXT Team, 2011, Mem. Soc. Astron. Ital. Supp., 17, 36
Burns J. O., Hallman E. J., Gantner B., Motl P. M., Norman M. L., 2008, ApJ, 675, 1125
Cappelluti N. et al., 2011, Mem. Soc. Astron. Ital. Supp., 17, 159
Croston J. H. et al., 2008, A&A, 487, 431
Dolag K., Jubelgas M., Springel V., Borgani S., Rasia E., 2004, ApJ, 606, L97
Dolag K., Vazza F., Brunetti G., Tormen G., 2005, MNRAS, 364, 753
Dolag K., Borgani S., Murante G., Springel V., 2009, MNRAS, 399, 497
Eke V. R., Cole S., Frenk C. S., 1996, MNRAS, 282, 263
Ettori S., Tozzi P., Borgani S., Rosati P., 2004, A&A, 417, 13
Ettori S., Dolag K., Borgani S., Murante G., 2006, MNRAS, 365, 1021
Evrard A. E., Metzler C. A., Navarro J. F., 1996, ApJ, 469, 494
Fabjan D., Borgani S., Tornatore L., Saro A., Murante G., Dolag K., 2010, MNRAS, 401, 1670
Gardini A., Rasia E., Mazzotta P., Tormen G., De Grandi S., Moscardini L., 2004, MNRAS, 351, 505
Gottloeber S., Yepes G., Wagner C., Sevilla R., 2006, preprint (astro-ph/0608289)
Grevesse N., Sauval A. J., 1998, Space Sci. Rev., 85, 161
Haardt F., Madau P., 1996, ApJ, 461, 20
Hartley W. G., Gazzola L., Pearce F. R., Kay S. T., Thomas P. A., 2008, MNRAS, 386, 2015
Henry J. P., Arnaud K. A., 1991, ApJ, 372, 410
Henry J. P., Evrard A. E., Hoekstra H., Babul A., Mahdavi A., 2009, ApJ, 691, 1307
Ikebe Y., Reiprich T. H., Böhringer H., Tanaka Y., Kitayama T., 2002, A&A, 383, 773
Jeltema T. E., Hallman E. J., Burns J. O., Motl P. M., 2008, ApJ, 681, 167
Jubelgas M., Springel V., Dolag K., 2004, MNRAS, 351, 423
Kaiser N., 1986, MNRAS, 222, 323
Kay S. T., da Silva A. C., Aghanim N., Blanchard A., Liddle A. R., Puget J.-L., Sadat R., Thomas P. A., 2007, MNRAS, 377, 317
Komatsu E. et al., 2011, ApJS, 192, 18
Kravtsov A. V., Nagai D., Vikhlinin A. A., 2005, ApJ, 625, 588
Kravtsov A. V., Vikhlinin A., Nagai D., 2006, ApJ, 650, 128
Lau E. T., Kravtsov A. V., Nagai D., 2009, ApJ, 705, 1129
Leccardi A., Molendi S., 2008, A&A, 486, 359
Lima M., Hu W., 2005, Phys. Rev. D, 72, 043006
Loken C., Norman M. L., Nelson E., Burns J., Bryan G. L., Motl P., 2002, ApJ, 579, 571
Mahdavi A., Hoekstra H., Babul A., Henry J. P., 2008, MNRAS, 384, 1567
Mantz A., Allen S. W., Ebeling H., Rapetti D., Drlica-Wagner A., 2010, MNRAS, 406, 1773
Markevitch M., 1998, ApJ, 504, 27
Maughan B. J., 2007, ApJ, 668, 772
Mazzotta P., Rasia E., Moscardini L., Tormen G., 2004, MNRAS, 354, 10
Monaghan J. J., 1997, J. Comput. Phys., 136, 298
Morris J. P., Monaghan J. J., 1997, J. Comput. Phys., 136, 41
Muanwong O., Kay S. T., Thomas P. A., 2006, ApJ, 649, 640
Nagai D., Vikhlinin A., Kravtsov A. V., 2007a, ApJ, 655, 98
Nagai D., Kravtsov A. V., Vikhlinin A., 2007b, ApJ, 668, 1
O'Hara T. B., Mohr J. J., Bialek J. J., Evrard A. E., 2006, ApJ, 639, 64
Okabe N., Zhang Y., Finoguenov A., Takada M., Smith G. P., Umetsu K., Futamase T., 2010, ApJ, 721, 875
Padovani P., Matteucci F., 1993, ApJ, 416, 26
Pierpaoli E., Borgani S., Scott D., White M., 2003, MNRAS, 342, 163
Piffaretti R., Valdarnini R., 2008, A&A, 491, 71
Poole G. B., Babul A., McCarthy I. G., Fardal M. A., Bildfell C. J., Quinn T., Mahdavi A., 2007, MNRAS, 380, 437
Pratt G. W., Böhringer H., Croston J. H., Arnaud M., Borgani S., Finoguenov A., Temple R. F., 2007, A&A, 461, 71
Pratt G. W., Croston J. H., Arnaud M., Böhringer H., 2009, A&A, 498, 361
Press W. H., Teukolsky S. A., Vetterling W. T., Flannery B. P., 1992, Numerical Recipes in C. The Art of Scientific Computing. Cambridge Univ. Press, Cambridge
Puchwein E., Sijacki D., Springel V., 2008, ApJ, 687, L53
Rasia E., Tormen G., Moscardini L., 2004, MNRAS, 351, 237
Rasia E., Mazzotta P., Borgani S., Moscardini L., Dolag K., Tormen G., Diaferio A., Murante G., 2005, ApJ, 618, L1
Rasia E., Mazzotta P., Bourdin H., Borgani S., Tornatore L., Ettori S., Dolag K., Moscardini L., 2008, ApJ, 674, 728
Rasia E., Mazzotta P., Evrard A., Markevitch M., Dolag K., Meneghetti M., 2011, ApJ, 729, 45
Reiprich T., Böhringer H., 2002, ApJ, 567, 716
Roncarelli M., Ettori S., Dolag K., Moscardini L., Borgani S., Murante G., 2006, MNRAS, 373, 1339

Salpeter E. E., 1955, ApJ, 121, 161
Schuecker P., Guzzo L., Collins C. A., Böhringer H., 2002, MNRAS, 335, 807
Shaw L. D., Holder G. P., Dudley J., 2010, ApJ, 716, 281
Short C. J., Thomas P. A., Young O. E., Pearce F. R., Jenkins A., Muanwong O., 2010, MNRAS, 408, 2213
Sijacki D., Springel V., 2006, MNRAS, 366, 397
Springel V., 2005, MNRAS, 364, 1105
Springel V., Hernquist L., 2003, MNRAS, 339, 289
Springel V., Di Matteo T., Hernquist L., 2005, MNRAS, 361, 776
Stanek R., Rasia E., Evrard A. E., Pearce F., Gazzola L., 2010, ApJ, 715, 1508
Steinmetz M., 1996, MNRAS, 278, 1005
Sun M., Voit G. M., Donahue M., Jones C., Forman W., Vikhlinin A., 2009, ApJ, 693, 1142
Sutherland R. S., Dopita M. A., 1993, ApJS, 88, 253
Tormen G., Bouchet F. R., White S. D. M., 1997, MNRAS, 286, 865
Tornatore L., Borgani S., Dolag K., Matteucci F., 2007, MNRAS, 382, 1050
Valdarnini R., 2011, A&A, 256, A158
Vikhlinin A., 2006, ApJ, 640, 710
Vikhlinin A. et al., 2003, ApJ, 590, 15
Vikhlinin A., Kravtsov A., Forman W., Jones C., Markevitch M., Murray S. S., Van Speybroeck L., 2006, ApJ, 640, 691
Vikhlinin A. et al., 2009a, ApJ, 692, 1033
Vikhlinin A. et al., 2009b, ApJ, 692, 1060
Voevodkin A., Vikhlinin A., 2004, ApJ, 601, 610
Voit G. M., 2005a, Adv. Space Res., 36, 701
Voit G. M., 2005b, Rev. Modern Phys., 77, 207
Yang H., Ricker P. M., Sutter P. M., 2009, ApJ, 699, 315
Yoshida N., Sheth R. K., Diaferio A., 2001, MNRAS, 328, 669
Zhang Y. et al., 2010, ApJ, 711, 1033

This paper has been typeset from a TEX/LATEX file prepared by the author.